

# WDR5 remodels NANOG condensates to drive transcriptional programs and sustain stem cell identity

Received: 16 July 2025

Accepted: 12 January 2026

Published online: 21 January 2026

 Check for updates

Duo Wang<sup>1,2,10</sup>, Xianle Shi<sup>3,10</sup>, Jiaying Xie<sup>1,4,10</sup>, Lijie Zhao<sup>2,10</sup>, Bin Wu<sup>5,10</sup>, Qiman Dong<sup>6</sup>, Yaoguang Huang<sup>2</sup>, Jinlong Suo<sup>7</sup>, Xinyu Wang<sup>1,4</sup>, Beixuan He<sup>1,4</sup>, Shukun Yan<sup>2</sup>, Hongjuan Xue<sup>8</sup>, Yuheng Shi<sup>9</sup>, Yingbin Liu<sup>1,4</sup>✉, Jianlong Wang<sup>3</sup>✉, Yong Chen<sup>2</sup>✉ & Yanjing Li<sup>1,4</sup>✉

Stem cell pluripotency relies on a finely tuned interplay between transcription factors and epigenetic regulators. Here, we identify a direct interaction between NANOG, a master pluripotency transcription factor, and WDR5, a core chromatin regulator essential for maintaining stem cell identity. Mechanistically, WDR5 remodels irregular NANOG aggregates into dynamic, liquid-liquid phase-separated condensates at pluripotency-associated promoters to activate target genes. Structural analyses show that the NANOG homeodomain engages WDR5 through an extended interface distinct from previously characterized short linear motifs. The NANOG R153A mutation disrupts this interaction, leading to impaired condensate formation, reduced chromatin co-occupancy, and diminished levels of active histone marks, ultimately compromising embryonic stem cell pluripotency. Pharmacological inhibition of the WDR5-NANOG interaction suppresses leukemia stem cell expansion in vivo, highlighting its therapeutic potential. Collectively, this study reveals that WDR5-dependent regulation of NANOG condensate dynamics links phase-separated assemblies to transcriptional control of stem cell identity in physiological and pathological contexts.

Stem cells possess the potential to maintain their pluripotent state, self-renew, and differentiate into specialized cell types<sup>1</sup>. These capabilities underpin their essential roles in embryonic development<sup>2</sup>, tissue regeneration<sup>3,4</sup>, and tumor progression<sup>5</sup>. Core transcription factors, such as NANOG, OCT4, and SOX2, play critical roles in maintaining pluripotency by orchestrating complex transcriptional programs<sup>6–8</sup>. Among them, NANOG stands out as a master regulator of pluripotency<sup>9–11</sup>. For instance, NANOG cooperates with BACH1 to recruit MLL/SET1 complexes, promoting H3K4me3 deposition and regulating enhancer-promoter activity critical for maintaining pluripotency<sup>12</sup>. Additionally, NANOG directly recruits BRG1, a catalytic subunit of the SWI/SNF chromatin remodeling complex, thereby facilitating transcription factor accessibility at critical pluripotency loci<sup>13</sup>.

NANOG comprises three domains: an intrinsically disordered N-terminal domain (NTD), a central structured DNA-binding homeodomain (HD), and a C-terminal domain (CTD) containing tryptophan repeats. While NANOG is well recognized to function as a transcription factor through its HD, emerging evidence suggests that both the NTD and CTD also play critical regulatory roles via their distinct structural features. The CTD was first reported to mediate NANOG homodimerization<sup>14</sup> and subsequently shown to form higher-order oligomers and fibrillar assemblies that promote DNA bridging and long-range chromatin interactions<sup>15</sup>. NANOG also forms phase-separated condensates, mediated by its NTD, with coactivators such as MED1 and BRD4 at super-enhancers, a process that facilitates the robust transcriptional activation for maintaining pluripotency in

A full list of affiliations appears at the end of the paper. ✉e-mail: [laoniulyb@shsmu.edu.cn](mailto:laoniulyb@shsmu.edu.cn); [jw3925@cumc.columbia.edu](mailto:jw3925@cumc.columbia.edu); [yongchen@sibcb.ac.cn](mailto:yongchen@sibcb.ac.cn); [liyanjing@sjtu.edu.cn](mailto:liyanjing@sjtu.edu.cn)

embryonic stem cells (ESCs)<sup>16,17</sup>. Additionally, NANOG-TAZ condensates specifically reinforce pluripotency-associated transcriptional programs in cancer stem cells (CSCs), thereby enhancing their stem-like properties and therapy resistance<sup>18</sup>. This liquid-liquid phase-separated (LLPS)-driven regulatory mechanism underscores NANOG's functional versatility, providing a unifying principle linking transcription factor dynamics and gene expression regulation across both physiological and pathological contexts.

Beyond transcription factors, epigenetic regulation constitutes another essential regulatory layer for maintaining pluripotency. The WD40 repeat protein WDR5 serves as a central hub that integrates chromatin modifications with transcription factor activity<sup>19</sup>. As a core component of both the SET1/MLL histone methyltransferase complexes<sup>20,21</sup> and the MOF acetyltransferase complex<sup>22,23</sup>, WDR5 mediates the establishment of active histone marks, including H3K4 methylation and H4K16 acetylation. WDR5 interacts with multiple transcription factors such as OCT4<sup>19</sup>, MYC<sup>24–26</sup>, SOX2<sup>27</sup>, and TOX3<sup>28</sup> to regulate transcriptional programs essential for stem cell identity and, under pathological conditions, contributes to oncogenic self-renewal and therapeutic resistance. WDR5 depletion perturbs active histone modifications, downregulates pluripotency genes, and compromises stem cell maintenance<sup>19,29</sup>. Furthermore, pharmacological inhibition of WDR5 has exhibited potent anti-tumor activity across diverse cancer types, further highlighting its therapeutic potential<sup>30–34</sup>. Through its scaffolding capacity, WDR5 coordinates transcription factors with chromatin-modifying complexes to establish a permissive epigenetic landscape critical for stem cell identity. Yet, how WDR5 engages transcription factors like NANOG at the molecular level, and whether WDR5 can actively modulate their LLPS behavior and downstream gene regulation, remain unclear.

In this study, we identify a direct interaction between NANOG and WDR5, mediated by a previously uncharacterized binding interface that is distinct from canonical WDR5-WIN motif interactions and involves a broad contact surface across NANOG's structured homeodomain. Mechanistically, WDR5 remodels  $\beta$ -sheet-enriched, irregular NANOG aggregates into dynamic, liquid-like condensates, thereby enhancing NANOG's chromatin recruitment and transcriptional activation at pluripotency-associated loci. NANOG R153A, a mutation which disrupts its interaction with WDR5, impairs LLPS formation, reduces active chromatin marks H3K4me3 and H4K16ac, and compromises the maintenance of pluripotency. Furthermore, pharmacological inhibition of the WDR5-NANOG interaction with the WDR5 WIN-motif inhibitor C16 significantly inhibits the expansion and self-renewal of leukemia stem cells (LSCs) in vivo, highlighting the therapeutic potential of targeting this axis in cancer.

## Results

### WDR5 binds NANOG and remodels its aggregation state

We identified an interaction between WDR5 and NANOG by co-immunoprecipitation (co-IP) in HEK293T cells co-transfected with both constructs (Fig. 1a) and confirmed their direct binding in vitro with purified proteins (Supplementary Fig. 1a-c). Notably, purified NANOG exhibited a propensity for aggregation on the size-exclusion chromatography (SEC) (Supplementary Fig. 1a, b), which is consistent with a previous report showing that its C-terminal domain (CTD) drives higher-order oligomerization<sup>15</sup>. We then asked whether WDR5 could modulate NANOG's structural behavior and aggregation propensity. To address this, we utilized electron microscopy (EM) to visualize purified proteins. While NANOG alone formed irregular, amorphous aggregates, the supplement of WDR5 induced a structural reorganization of NANOG, resulting in the formation of droplet-like structures that displayed characteristic features of LLPS (Fig. 1b, c).

To explore the molecular basis underlying this transition, we performed protein structure predictions using AlphaFold<sup>35</sup> and analyzed intrinsic disorder characteristics using PONDR<sup>36</sup>. These analyses

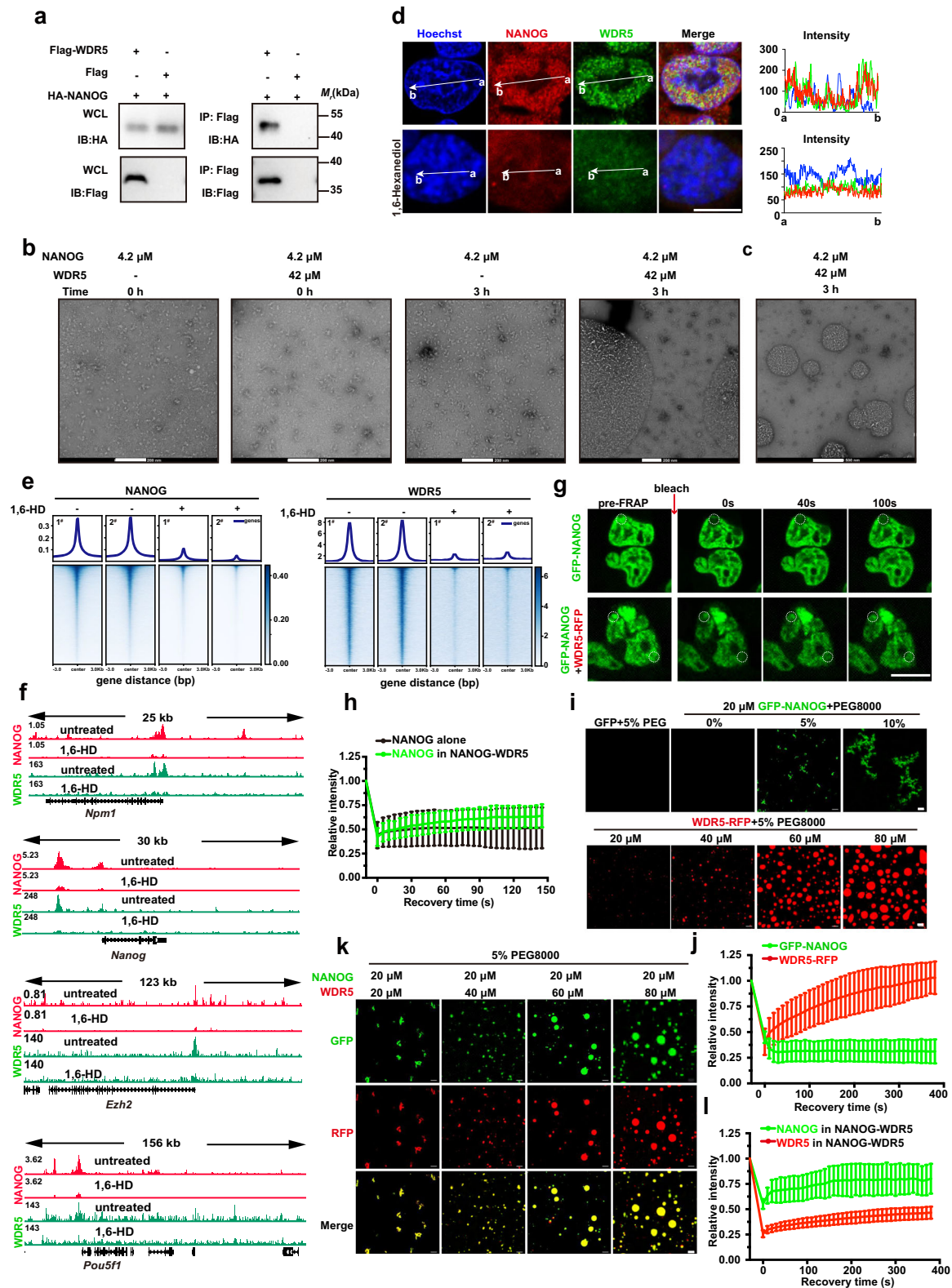
identified two intrinsically disordered regions (IDRs) in NANOG: a prominent IDR at its NTD and a distinct IDR at its CTD, the latter of which contains tryptophan-repeat motifs implicated in NANOG self-assembly<sup>15</sup> (Supplementary Fig. 1d, e). Notably, WDR5 also features a disordered NTD, a structural feature commonly observed in proteins with phase separation potential. These predictive analyses, combined with our EM observations, suggest that WDR5 may modulate NANOG's structural dynamics by promoting LLPS.

To validate these findings in vivo, we generated a Flag-tagged WDR5 knock-in androgenetic haploid embryonic stem cell (AG-haESC) line using CRISPR-Cas9 technology<sup>37–39</sup>. These cells can undergo spontaneous diploidization, allowing the rapid generation of homozygous mutations (Supplementary Fig. 1f). There was a substantial overlap between endogenous NANOG and WDR5 within nuclear puncta, indicative of biomolecular condensate formation in mESCs (Fig. 1d). These condensates rapidly dissolved upon treatment with 1,6-hexanediol (1,6-HD), a well-characterized disruptor of LLPS (Fig. 1d). Chromatin immunoprecipitation sequencing (ChIP-seq) of WDR5 and NANOG further demonstrated a global reduction in peak intensities upon 1,6-HD treatment, reflecting a widespread decrease in their chromatin occupancy (Fig. 1e). Additionally, ChIP-seq signals at key pluripotency genes, including *Npm1*, *Nanog*, *Ezh2*, and *Pou5f1*, were markedly reduced, suggesting that WDR5-NANOG phase-separated condensates may be crucial for sustaining their occupancy at pluripotency genes (Fig. 1f).

We next performed fluorescence recovery after photobleaching (FRAP) experiments to further characterize the dynamic properties of WDR5-NANOG condensates. In HEK293A cells transiently transfected with green fluorescent protein (GFP)-tagged NANOG and red fluorescent protein (RFP)-tagged WDR5 constructs, the two proteins showed strong co-localization in nuclear puncta (Supplementary Fig. 1g). FRAP analysis showed that GFP-NANOG puncta in co-transfected cells displayed partial fluorescence recovery within minutes, indicative of dynamic, liquid-like properties (Fig. 1g, h). In contrast, GFP-NANOG expressed alone exhibited negligible fluorescence recovery, suggesting the formation of solid-like condensates with impaired molecular dynamics (Fig. 1g, h).

Given the complexity of intracellular environments, we conducted in vitro phase separation assays using purified GFP-NANOG and WDR5-RFP proteins. Consistent with our EM observations, GFP-NANOG alone formed irregular aggregates, while WDR5-RFP exhibited weak LLPS that became more pronounced at concentrations above 40  $\mu$ M (Fig. 1i). WDR5-RFP droplets exhibited rapid fluorescence recovery, while GFP-NANOG aggregates remained static, indicating a lack of fluidity (Fig. 1j). Notably, the addition of WDR5 induced a concentration-dependent transition of NANOG from irregular aggregates to liquid-like droplets (Fig. 1k), and this transition was confirmed by FRAP (Fig. 1l). In addition, a truncated NANOG 1-155 construct lacking the C-terminal domain failed to form condensates even under crowding conditions, highlighting a critical role of the CTD in NANOG aggregation (Supplementary Fig. 1h).

To gain molecular insights into this phenomenon, we employed AlphaFold3-based structural modeling to predict the structural organization of NANOG alone and in complex with WDR5 at varying molecular stoichiometries. In multimeric NANOG models (4, 8, and 16 molecules), the C-terminal region progressively adopted  $\beta$ -sheet-enriched stacking structures characteristic of aggregation (Supplementary Fig. 2a). In contrast, structural modeling of WDR5-NANOG complexes (1, 4, and 8 molecules) indicated that WDR5 binding imposes steric constraints that hinder  $\beta$ -sheet formation at the NANOG C-terminus, thereby reducing the propensity for aggregated states (Supplementary Fig. 2b). This predicted disruption of  $\beta$ -sheet assembly is consistent with the experimentally observed shift toward dynamic, liquid-like condensates in the presence of WDR5, providing a structural rationale for its role in promoting phase separation.



### WDR5 binds directly to the NANOG homeodomain

Next, we sought to identify the region within NANOG that was responsible for its interaction with WDR5. Domain mapping by co-IP in HEK293T cells showed that WDR5 specifically binds the N-terminal fragment of NANOG (residues 1-155), but not the C-terminal fragment (residues 155-305) (Fig. 2a). To further define the minimal binding region, we conducted isothermal titration calorimetry (ITC) assays

using shorter NANOG fragments: residues 1-96, 91-104, 96-155, and 101-155 (Fig. 2b). Among them, only the 96-155 fragment exhibited significant affinity for WDR5, with a dissociation constant of  $5.13 \pm 0.03 \mu\text{M}$ , whereas no detectable binding was observed for the other fragments (Fig. 2c). These results define residues 96-155, which contain the complete homeodomain (HD), as the minimal region mediating the WDR5-NANOG interaction.

**Fig. 1 | WDR5 interacts with NANOG to facilitate its liquid-liquid phase**

**separation.** **a** Co-immunoprecipitation (co-IP) of Flag-WDR5 and HA-NANOG in co-transfected HEK293T cells. Cell lysates were immunoprecipitated (IP) with anti-Flag beads and analyzed by immunoblotting (IB) with anti-HA and anti-FLAG antibodies. WCL, whole-cell lysate. Negative-stain electron microscopy images of full-length NANOG alone or mixed with WDR5 at 0 h and 3 h of incubation in 25 mM Tris-HCl (pH 8.0) and 150 mM NaCl. Scale bars, 200 nm (**b**) and 500 nm (**c**).

**d** Immunofluorescence staining of mESCs with endogenous NANOG and C-terminal FLAG-tagged WDR5 (knock-in), before and after treatment with 3% 1,6-hexanediol for 15 min. NANOG and WDR5 were detected with distinct antibodies, and nuclei were counterstained with Hoechst. Scale bars, 10 μm. **e** Heatmaps of ChIP-seq signals for NANOG and WDR5 across ±3 kb from peak centers in mESCs under untreated or 3% 1,6-hexanediol-treated conditions (15 min). 1<sup>#</sup> and 2<sup>#</sup> indicate independent biological replicates. **f** ChIP-seq tracks of NANOG and WDR5 at representative pluripotency loci in control and 1,6-hexanediol-treated mESCs. **g** Representative fluorescence recovery after photobleaching (FRAP) images of

exogenously expressed GFP-NANOG alone or co-expressed with WDR5-RFP in HEK293A cells. Scale bars, 10 μm. **h** Quantification of FRAP recovery for GFP-NANOG alone or within WDR5-NANOG condensates (related to Fig. 1g). Data are mean ± SD of *n* = 20 droplets from three independent experiments. **i** In vitro droplet formation of GFP-NANOG with increasing concentrations of PEG8000, and WDR5-RFP with increasing protein concentrations in the presence of 5% PEG8000. Droplet assays were performed in 25 mM Tris-HCl (pH 8.0) and 150 mM NaCl. Scale bars, 10 μm. **j** FRAP recovery curves of 20 μM GFP-NANOG and 60 μM WDR5-RFP droplets in 5% PEG8000 (related to Fig. 1i). Data are mean ± SD of *n* = 15 droplets from 3 independent experiments. **k** Representative fluorescence microscopy images showing droplet formation in mixtures of GFP-NANOG and WDR5-RFP with molar ratios from 1:1 to 1:4. Scale bars, 10 μm. **l** FRAP recovery curves of co-condensates formed by 20 μM GFP-NANOG and 60 μM WDR5-RFP (related to Fig. 1k). Data are mean ± SD of *n* = 15 droplets from three independent experiments. Source data are provided as a Source Data file.

The crystal structure of NANOG HD domain<sup>40</sup> shows that the residues 96-155 of NANOG comprise an unstructured loop (96-104) followed by three structured α-helices (104-155) (Supplementary Fig. 3a). Interestingly, WDR5 is well-documented to interact with proteins such as MLL/SET methyltransferases, RBBP5, KANSL1, and KANSL2 via its WIN (WDR5-interacting) and WBM (WDR5-binding) pockets, typically engaging short loop sequences (Supplementary Fig. 3b, c). However, unlike these canonical interactions, the NANOG binding region encompasses both an unstructured loop and adjacent α-helices, indicating a previously unrecognized mechanism of WDR5 engagement.

To assess the specificity of the WDR5-NANOG interaction, we examined other NKL subclass homeodomain transcription factors, including HLX, DLX1, HHEX, and BARX1<sup>41</sup>. Binding assays (ITC) demonstrated variable affinities: HLX showed relatively high-affinity binding ( $K_d = 4.13 \mu\text{M}$ ), DLX1 exhibited a weaker interaction ( $K_d = 206.2 \mu\text{M}$ ), whereas HHEX and BARX1 lacked detectable binding (Supplementary Fig. 3d). Sequence alignment showed that the homeodomain is relatively conserved between mouse and human orthologs but displays limited conservation across NKL subclass members (Fig. 2d). These findings highlight the specificity of the WDR5-NANOG interaction, suggesting that it represents a structurally distinct and sequence-dependent binding paradigm.

**Molecular basis of the WDR5-NANOG interaction**

To elucidate the molecular basis underlying the interaction between NANOG and WDR5, we determined the crystal structure of NANOG HD in complex with WDR5 using X-ray crystallography. Initial crystallization trials using various NANOG truncations bound to WDR5 failed to yield diffracting crystals; we therefore engineered a series of NANOG mutants designed to retain WDR5-binding activity while enhancing crystallization efficiency. Among these mutants, NANOG HD<sup>R100A</sup> successfully formed high-quality crystals in complex with WDR5, allowing for the determination of its structure at a 2.5 Å resolution (Fig. 3a, Supplementary Fig. 4a, Table 1). The NANOG HD<sup>R100A</sup> mutation did not significantly affect its binding affinity to WDR5, with a  $K_d$  value of approximately 5.78 μM, comparable to that of the wild-type NANOG homeodomain (Supplementary Fig. 4b). Additionally, the NANOG HD<sup>R100A</sup> also formed a stable heterodimeric complex with WDR5 in solution (Supplementary Fig. 4c).

Structural analysis showed that both the N-terminal arm and the C-terminal region of NANOG HD mediate the interaction with WDR5 (Fig. 3b, c). At the N terminus, the side-chain amine groups of NANOG K96 and K98 form electrostatic interactions and hydrogen bonds with WDR5 D213 and D192, respectively. Additionally, Q97 participates in a water-mediated hydrogen bond with WDR5 residue N214 (Fig. 3b). The C-terminal region of NANOG HD engages WDR5 through a network of

extensive hydrophobic interactions and hydrogen bonds, thereby establishing a stable interaction interface (Fig. 3c, d).

Like previously characterized complexes such as WDR5-MLL1 and WDR5-KANSL1, the C-terminal region of NANOG HD interacts with WDR5 through the insertion of a key arginine residue, R153, into WDR5's central channel (Fig. 3c, d, Supplementary Fig. 4d). R153 establishes extensive interactions with WDR5: the amine nitrogen of R153 forms hydrogen bonds with WDR5 residues S91, F133, and C261, while its guanidinium group engages in cation-π interactions with the aromatic side chains of WDR5 residues F133 and F263 (Fig. 3d). However, unlike the canonical WIN motif, which typically consists of a tetrapeptide sequence (A-R[position 0]-[A/C/S/T]-[E/K/R]) with conserved arginine (position 0) and alanine (position -1) residues critical for interaction<sup>42</sup> (Supplementary Fig. 3c), the surrounding NANOG sequence is far less conserved. Notably, in NANOG, the residue at position -1 is K, which does not contribute to the interaction interface. Instead, residues at position -2 (C) and position +1 (W) form new interaction pockets with WDR5, thereby defining a noncanonical and previously unrecognized binding mode (Fig. 3c).

To validate whether the interaction observed in the crystal structure persists under physiological conditions, we employed nuclear magnetic resonance (NMR) spectroscopy experiments. For backbone resonance assignment, we prepared <sup>15</sup>N/<sup>13</sup>C-labeled NANOG HD and <sup>15</sup>N/<sup>13</sup>C/<sup>2</sup>H-labeled WDR5, enabling residue-specific peak mapping (Supplementary Fig. 4e, f). Subsequently, titration of unlabeled WDR5 into <sup>15</sup>N-labeled NANOG HD, and vice versa, yielded <sup>15</sup>N-<sup>1</sup>H heteronuclear single quantum coherence (HSQC) spectra that revealed distinct chemical shift perturbations upon complex formation (Supplementary Fig. 4g-i). Residue-level analysis indicated that WDR5's central channel and adjacent surface regions are involved in binding NANOG HD, while both the N-terminal arm and C-terminal region of NANOG HD participate in the interaction with WDR5 (Fig. 3e). Key residues, including Q97, K98, and R153 in NANOG, and F133 and D192 in WDR5, exhibited pronounced chemical shifts, consistent with their involvement in the crystal interface (Supplementary Fig. 4h, i). The strong correlation between the chemical shift perturbation patterns and the crystallographic interface provides compelling evidence that the interaction observed in the crystal structure is accurately recapitulated in solution.

We then introduced site-directed mutations at key contact residues and assessed their effects on binding to functionally validate the structural interface. Mutations such as NANOG<sup>R153A</sup>, WDR5<sup>F133A</sup>, and WDR5<sup>F263A</sup> significantly impaired binding affinity, whereas NANOG<sup>K96A</sup> and NANOG<sup>K98A</sup> caused only a modest decrease (Fig. 3f). Consistent with these in vitro findings, the R153A mutation in full-length NANOG markedly impaired its interaction with WDR5 in HEK293T cells

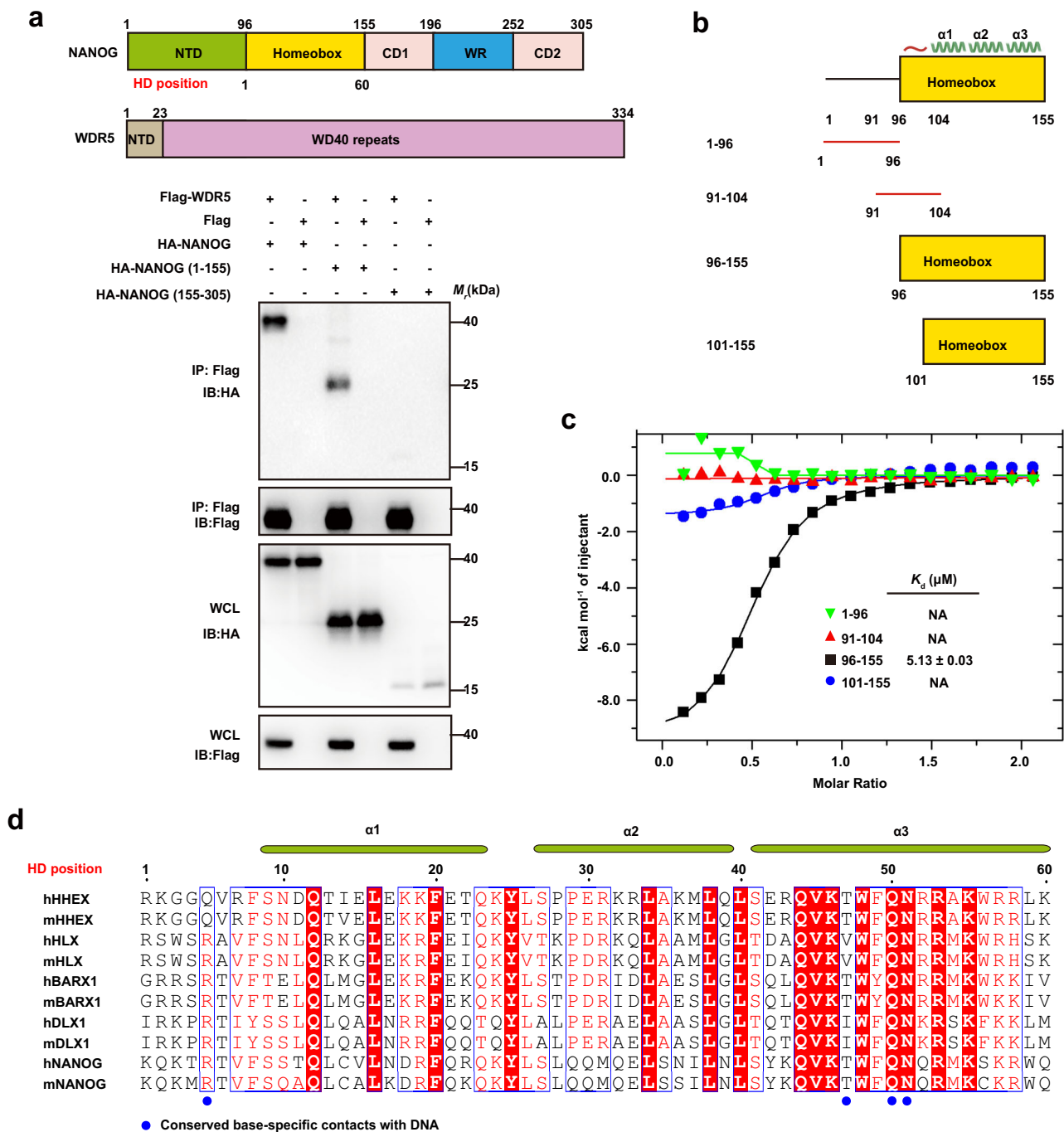


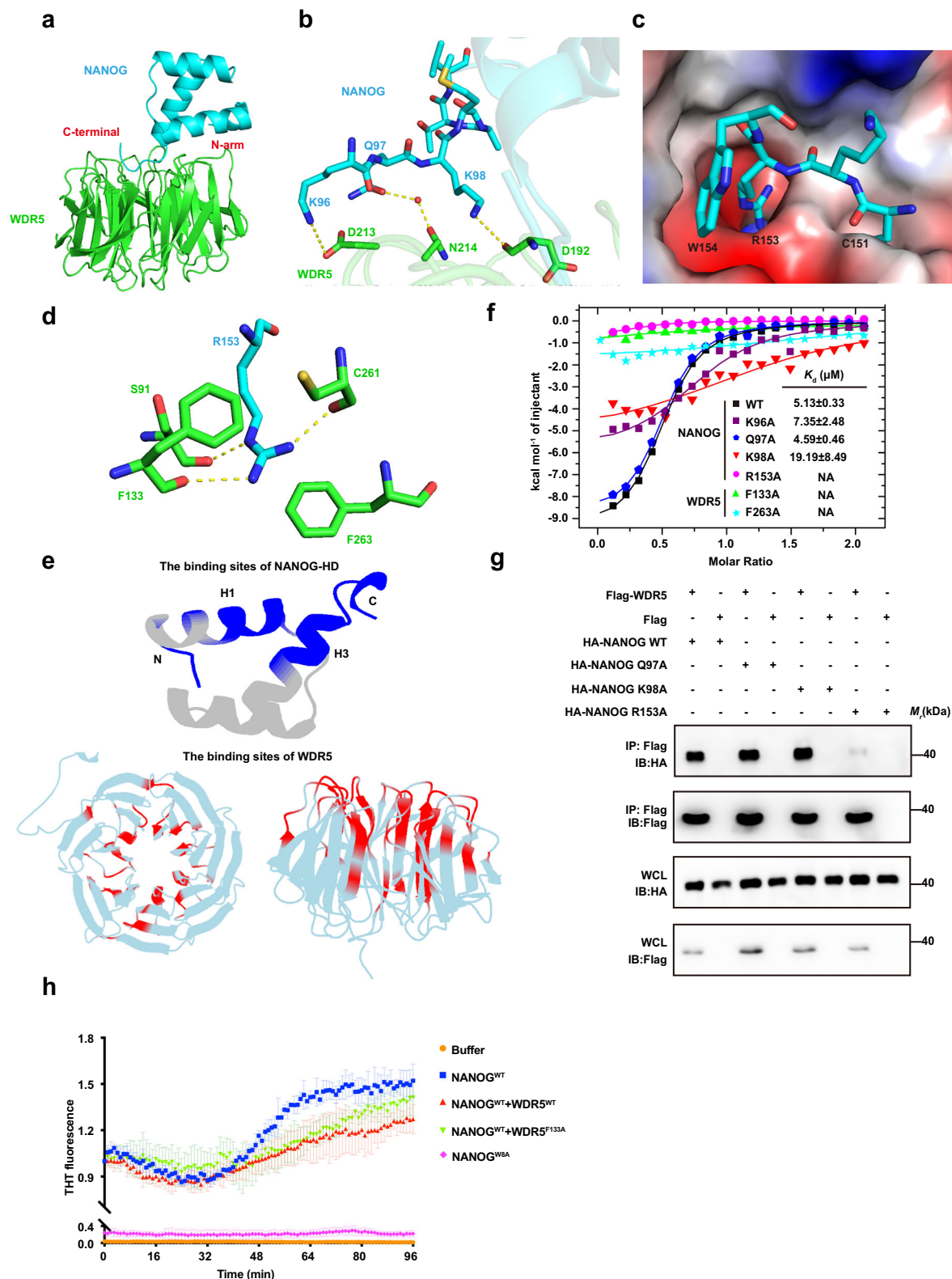
**Fig. 2 | WDR5 binds directly to the homeodomain of NANOG.** **a** Domain mapping of NANOG to identify WDR5-interacting regions by co-IP. Full-length and truncated HA-NANOG constructs (residues 1-155 and 155-305) were co-transfected with FLAG-WDR5 in HEK293T cells. Schematic at the top shows the domain organization of NANOG and WDR5. **b** Schematic representation of NANOG truncations used for isothermal titration calorimetry (ITC), including the N-terminal region (1-96), the full homeodomain (96-155, HD), an N-terminal loop segment of HD (91-104), and the core HD region comprising the three  $\alpha$ -helices (101-155). Created in BioRender.

Shi, Y. (2026) <https://BioRender.com/h76z570>. **c** ITC analysis of WDR5 binding to various NANOG fragments. The homeodomain exhibited specific binding to WDR5 with a dissociation constant of  $5.13 \pm 0.03 \mu\text{M}$ , while other fragments (1-96, 91-104, 101-155) showed no detectable binding. **d** Multiple sequence alignment of the homeodomain regions from representative NKL-class homeodomain proteins in mouse and human. Residues are numbered according to canonical HD positions. Conserved base-specific contacts with DNA are indicated by blue dots. Source data are provided as a Source Data file.

(Fig. 3g). These data highlight the essential roles of hydrophobic and electrostatic interactions in stabilizing the WDR5-NANOG complex and provide physiological support for the crystallographic model.

To assess how WDR5 binding influences the assembly behavior of NANOG, we performed Thioflavin-T (ThT) kinetic assays to monitor the formation and modulation of  $\beta$ -sheet-enriched aggregates. NANOG<sup>WT</sup> showed a time-dependent increase in ThT fluorescence,

whereas the CTD mutant NANOG<sup>W8A</sup> displayed substantially lower ThT signal (Fig. 3h), consistent with previous studies indicating that the CTD promotes NANOG aggregation<sup>14,15</sup>. Addition of WDR5<sup>WT</sup> suppressed the ThT signal of NANOG<sup>WT</sup>, whereas the binding-impaired mutant WDR5<sup>F133A</sup> exhibited a weaker effect (Fig. 3h), consistent with our structural data and supporting a model in which WDR5 engages NANOG to remodel its  $\beta$ -sheet-enriched assemblies.



Given that the NANOG homeodomain also mediates DNA binding, we next asked whether WDR5 engagement is compatible with DNA binding. Structural superposition of the WDR5-NANOG HD complex with the DNA-bound NANOG HD<sup>43</sup> revealed a steric clash between WDR5 and the DNA duplex at the canonical recognition helix of NANOG HD, indicating that WDR5 and DNA likely compete for an overlapping binding surface on NANOG HD (Supplementary Fig. 5a). Electrophoretic mobility shift (EMSA) assays further confirmed that

NANOG HD bound the target DNA with high affinity and that WDR5 progressively disrupted NANOG-DNA complex formation in a concentration-dependent manner (Supplementary Fig. 5b). Interestingly, under molecular crowding conditions, WDR5, NANOG, and DNA can co-partition into tripartite phase-separated condensates (Supplementary Fig. 5c), suggesting that although WDR5 and DNA binding to an individual NANOG homeodomain are mutually exclusive in a strict structural sense, they can nonetheless coexist within higher-order

**Fig. 3 | Structural and biochemical characterization of the WDR5–NANOG HD interaction.** **a** Crystal structure of the WDR5–NANOG HD complex. The complex was crystallized using the R100A mutant of NANOG HD and a truncated WDR5 (23–334). NANOG HD and WDR5 are shown in cyan and green, respectively. **b** Detailed interactions between the N-arm of NANOG HD and WDR5. Hydrogen bonds are indicated by yellow dashed lines, and key residues are shown as ball-and-stick models. A water molecule involved in the interaction is shown in red. **c** Detailed interactions between the C-terminal region of NANOG HD and WDR5. WDR5 is shown as an electrostatic surface, and interacting residues of NANOG HD are displayed as sticks. **d** Close-up view of the interaction between NANOG HD residue

R153 and surrounding residues in WDR5. **e** NMR mapping of the WDR5–NANOG HD interface. Binding sites of NANOG HD and WDR5 are indicated in blue and red, respectively. **f** ITC binding curves for wild-type and mutant forms of NANOG HD and WDR5. Mutations at the binding interface markedly reduced or abolished the interaction. **g** Co-IP showing the interaction between full-length WDR5 and various full-length NANOG mutants. **h** The kinetics of full length NANOG<sup>WT</sup>, NANOG<sup>WT</sup> + WDR5<sup>WT</sup>, NANOG<sup>WT</sup> + WDR5<sup>F133A</sup>, and NANOG<sup>W5A</sup>, measured using 5 μM NANOG and a 2:1 molar ratio of WDR5:NANOG; Buffer + ThT served as control. Traces show normalized ThT fluorescence over time. Data are mean ± SD from three independent experiments. Source data are provided as a Source Data file.

**Table 1 | Data collection and refinement statistics (molecular replacement)**

NANOG HD <sup>R100A</sup> –WDR5	
<b>Data collection</b>	
Space group	P 1 2 <sub>1</sub> 1
Cell dimensions	
a, b, c (Å)	85.67, 87.60, 96.87
α, β, γ (°)	90.00, 91.81, 90.00
Wavelength (Å)	0.9785
Resolution (Å)	50.00–2.50
R <sub>merge</sub>	0.179 (0.650) <sup>a</sup>
I/σI	8.1 (2.1)
Completeness (%)	99.9 (99.9)
Redundancy	6.8 (6.9)
<b>Refinement</b>	
Resolution (Å)	37.57–2.50
No. reflections	49282
R <sub>work</sub> /R <sub>free</sub> (%)	17.36/22.14
No. atoms	
Protein	8018
Water	293
B-factors (Å <sup>2</sup> )	
Protein	22.79
Water	23.31
R.m.s deviations	
Bond lengths (Å)	0.008
Bond angles (°)	0.973

<sup>a</sup>Values in parentheses are for the highest-resolution shell.

condensates, likely through multivalent, dynamic interactions. This co-condensation is likely concentration-dependent and may be facilitated by the dynamic assembly properties of phase-separated condensates, which can accommodate partially competing binding events via multivalent interactions.

### Disrupting WDR5–NANOG binding impairs mESC pluripotency

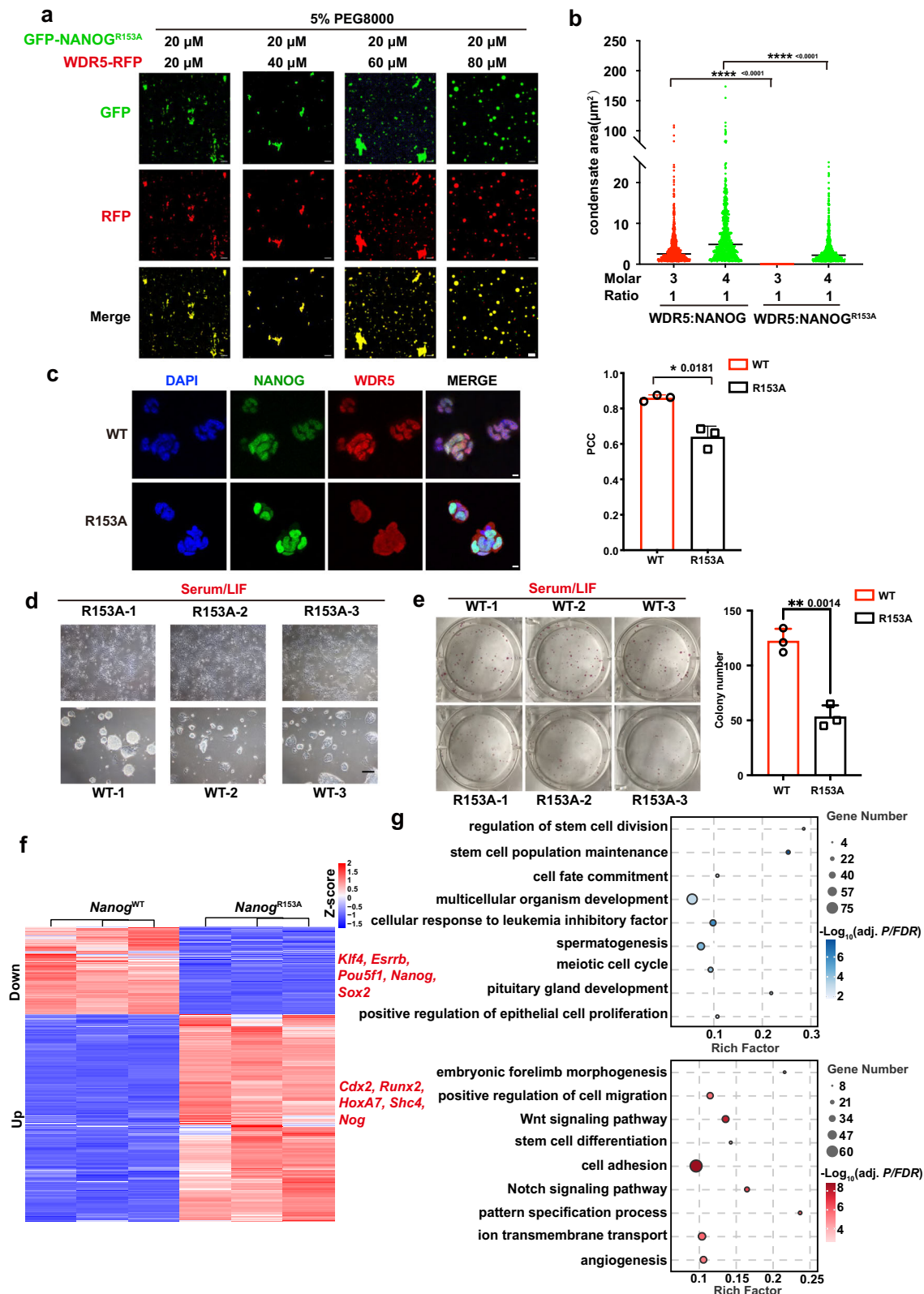
To elucidate the functional significance of the WDR5–NANOG interaction, we utilized the NANOG<sup>R153A</sup> mutant, which specifically disrupts WDR5 binding while preserving NANOG's DNA-binding ability under physiological salt conditions (Supplementary Fig. 5d, e). This mutation served as an ideal model to dissect the specific contributions of the WDR5–NANOG interaction. The purified GFP–NANOG<sup>R153A</sup>, like GFP–NANOG<sup>WT</sup>, formed high-molecular-weight aggregates, indicating that this mutation does not intrinsically affect NANOG's self-assembly propensity (Supplementary Fig. 5f, g). However, GFP–NANOG<sup>R153A</sup> retained its intrinsic fibrillar state and failed to transition into liquid-like condensates upon the addition of WDR5–RFP (Fig. 4a, Supplementary Fig. 5h), under conditions that readily induced LLPS in GFP–NANOG<sup>WT</sup> (Fig. 1k, l). When the concentration of WDR5–RFP was

increased to 80 μM (a fourfold molar excess over GFP–NANOG<sup>R153A</sup>), phase separation was partially restored, albeit forming fewer and smaller condensates (Fig. 4a) compared to GFP–NANOG<sup>WT</sup> (Fig. 1k). Quantitative analysis of droplet condensate areas further confirmed that the LLPS capacity of GFP–NANOG<sup>R153A</sup> was markedly diminished, even at elevated WDR5–RFP concentrations, highlighting the pivotal role of the WDR5–NANOG interaction in reshaping NANOG's conformational state (Fig. 4b).

We next investigated whether the WDR5–NANOG interaction is essential for the pluripotency of mESCs. We generated NANOG<sup>R153A</sup> knock-in mESC lines (Supplementary Fig. 6a) and initially cultured them under conditions that support pluripotency (2i medium). We then transferred the cells to serum/LIF medium, a relatively weaker condition for pluripotency maintenance, to evaluate the effect of disrupting the WDR5–NANOG interaction on mESC self-renewal. Immunofluorescence analysis revealed reduced co-localization between WDR5 and NANOG<sup>R153A</sup> compared to NANOG<sup>WT</sup>, as quantified by Pearson's correlation coefficient (Fig. 4c). Meanwhile, NANOG<sup>R153A</sup> mESCs exhibited striking morphological changes, transitioning from compact, dome-shaped colonies to flattened, irregular colonies indicative of differentiation (Fig. 4d). These morphological changes were accompanied by reduced alkaline phosphatase (AP) staining, a classical marker of pluripotency, as well as a marked reduction in colony number, indicating an impaired self-renewal capacity of these NANOG<sup>R153A</sup> cells compared to NANOG<sup>WT</sup> mESCs (Fig. 4e). Given these defects in self-renewal, we next examined whether early lineage specification was altered using embryoid body (EB) differentiation assays. R153A mutant cells displayed increased expression of somatic lineage markers relative to WT cells, whereas the expression of primordial germ cell (PGC) markers was reduced, consistent with previous findings that NANOG is required not only to maintain pluripotency but also to promote PGC specification<sup>44</sup> (Supplementary Fig. 6b).

To dissect how the WDR5–NANOG interaction regulates mESC pluripotency at the transcriptional level, we performed RNA sequencing (RNA-seq) analysis comparing NANOG<sup>WT</sup> and NANOG<sup>R153A</sup> mESCs under serum/LIF culture. Remarkably, disruption of the WDR5–NANOG interface induced widespread transcriptional reprogramming, affecting 3,710 genes, including 1,131 downregulated and 2,579 upregulated genes (Fig. 4f, Supplementary Fig. 6c). Core pluripotency factors, such as *Klf4*, *Esrrb*, *Sox2*, and *Nanog* itself, were significantly repressed in NANOG<sup>R153A</sup> mESCs, establishing a link between the WDR5–NANOG interaction and the regulation of pluripotency genes. Conversely, genes associated with differentiation and lineage commitment, including *Runx2*, *Hoxa7*, and *Shc4*, were robustly upregulated, reflecting a pronounced shift towards differentiation (Fig. 4f, Supplementary Fig. 6c). Gene Ontology (GO) analysis further revealed that downregulated genes were enriched in pathways related to stem cell population maintenance, stem cell division, and cell fate commitment, while upregulated genes were associated with developmental processes, including embryonic forelimb morphogenesis, stem cell differentiation, and cellular adhesion (Fig. 4g).

Collectively, these results demonstrate that the WDR5–NANOG interaction is a critical molecular switch in safeguarding mESC identity



by stabilizing the core pluripotency network and preventing premature activation of lineage-specific differentiation programs.

### Loss of WDR5–NANOG interaction impairs active chromatin

We then used ChIP-seq to identify how the physical interaction between NANOG and WDR5 influences their genome-wide chromatin occupancy. The analyses were performed in both NANOG<sup>WT</sup> and

NANOG<sup>R153A</sup> mESCs cultured in serum/LIF to compare the binding profiles of NANOG and WDR5. We found that both NANOG and WDR5 were predominantly enriched at promoter regions, rather than enhancers, although the signals were substantially reduced in the mutant relative to wild-type mESCs (Supplementary Fig. 7a). Motif enrichment analyses confirmed that NANOG<sup>WT</sup>- and NANOG<sup>R153A</sup>-bound regions were similarly enriched for its own canonical motifs as well as

**Fig. 4 | NANOG R153A mutation impairs phase separation and compromises transcriptional control of ESC pluripotency.** **a** Representative fluorescence microscopy images showing droplet formation in GFP-NANOG<sup>R153A</sup> and WDR5-RFP mixtures at increasing molar ratios ranging from 1:1 to 1:4. Droplet assays were performed in buffer containing 25 mM Tris-HCl (pH 8.0), 150 mM NaCl, and 5% PEG8000. Scale bars, 10  $\mu$ m. **b** Quantification of condensate areas formed by WDR5 with NANOG<sup>WT</sup> (related to Fig. 1k) or NANOG<sup>R153A</sup> (related to Fig. 4a). Each dot represents one condensate, and horizontal lines indicate the median.  $n = 727$  droplets per condition, pooled from three independent experiments. \*\*\*\* $P < 0.0001$  by unpaired two-sided t-test. **c** Representative immunofluorescence images of NANOG (green) and WDR5 (red) in NANOG<sup>WT</sup> and NANOG<sup>R153A</sup> mESCs 2 h after withdrawal from 2i/LIF. Right, quantification of NANOG-WDR5 co-localization by Pearson's correlation coefficient (PCC). Data are mean  $\pm$  SD from three independent replicates (analyzing a total of 272 NANOG<sup>WT</sup> and 344 NANOG<sup>R153A</sup> cells). \* $P < 0.05$  by unpaired two-sided t-test. Scale bars, 10  $\mu$ m. **d** Phase-contrast microscopy images of mESCs endogenously expressing NANOG<sup>WT</sup> or NANOG<sup>R153A</sup>, cultured in serum/LIF

medium for 48 h following withdrawal from 2i medium. Scale bars, 100  $\mu$ m. **e** Alkaline phosphatase (AP) staining and quantification of mESC colonies expressing NANOG<sup>WT</sup> or NANOG<sup>R153A</sup> after 48 h in serum/LIF medium in 6-well plates. Data are mean  $\pm$  SD from three independent replicates. \*\* $P < 0.01$  by unpaired two-sided t-test. **f** Heatmap showing differentially expressed genes in mESCs expressing NANOG<sup>WT</sup> or NANOG<sup>R153A</sup>. Genes were identified by RNA-seq using  $|\log_2[\text{fold change}]| \geq 1$  and false discovery rate (FDR)  $< 0.05$  (Benjamini-Hochberg) as thresholds. Z-scores represent gene-wise normalized expression across samples. Data are from three independent biological replicates per genotype. **g** Gene ontology (GO) enrichment analysis of differentially expressed genes in NANOG<sup>R153A</sup> mESCs relative to NANOG<sup>WT</sup>, analyzed with DAVID. Downregulated and upregulated gene sets were tested separately using a one-sided hypergeometric test, and  $P$  values were adjusted with the Benjamini-Hochberg method (FDR). Dot size indicates gene number and color indicates  $-\log_{10}$  (adjusted  $P$  value). Source data are provided as a Source Data file.

those of other core pluripotency transcription factors, including OCT4, SOX2, and KLF4. A similar motif pattern was observed in WDR5-bound regions in NANOG<sup>WT</sup>, supporting the coordinated recruitment of these two proteins to shared regulatory elements. In contrast, WDR5-bound regions in NANOG<sup>R153A</sup> mESCs lacked most pluripotency motifs, except for c-MYC, suggesting partial redirection of WDR5 by other transcription factors in the absence of NANOG interaction (Supplementary Fig. 7b). Importantly, genome-wide profiling data further demonstrated that both NANOG and WDR5 binding signals were significantly diminished at shared co-occupied loci in NANOG<sup>R153A</sup> mESCs (Fig. 5a, b). Specifically, there was a marked reduction in co-occupied peaks, from 7796 in NANOG<sup>WT</sup> mESCs to only 143 in NANOG<sup>R153A</sup> mESCs (Fig. 5c). Moderate signal reductions were also observed at their respective unique binding sites (Fig. 5a, b), likely reflecting secondary effects from transcriptional reprogramming and partial differentiation in the mutant background. Despite these changes in binding intensity, the overall genomic distribution of binding sites remained largely unchanged, with promoter and distal intergenic regions still representing the major binding compartments of WDR5 and NANOG in NANOG<sup>R153A</sup> mESCs (Supplementary Fig. 7c).

To identify target genes co-bound and co-regulated by NANOG and WDR5, we integrated ChIP-seq and RNA-seq datasets in mESCs. Specifically, we intersected 7796 genes co-bound by NANOG and WDR5 with 3710 differentially expressed genes (DEGs) identified in NANOG<sup>R153A</sup> mESCs, resulting in 2087 genes affected by the disruption of WDR5-NANOG interaction (Fig. 5d). Further analysis revealed that 113 genes exhibited increased binding and upregulated expression, while 96 genes showed decreased binding and downregulated expression. The remaining 1878 genes displayed no significant binding changes but still exhibited transcriptional changes, likely through indirect regulation. Enrichment analysis indicated that genes with significant binding changes also showed statistically significant expression differences, whereas DEGs without binding changes did not exhibit significant expression differences (Fig. 5e). Genes with reduced binding were enriched for pathways essential for stem cell maintenance and pluripotency, such as embryonic pattern specification and cellular response to leukemia inhibitory factor (LIF). In contrast, genes with increased binding were associated with differentiation-related processes, including apoptotic signaling and Wnt pathway activation (Fig. 5f).

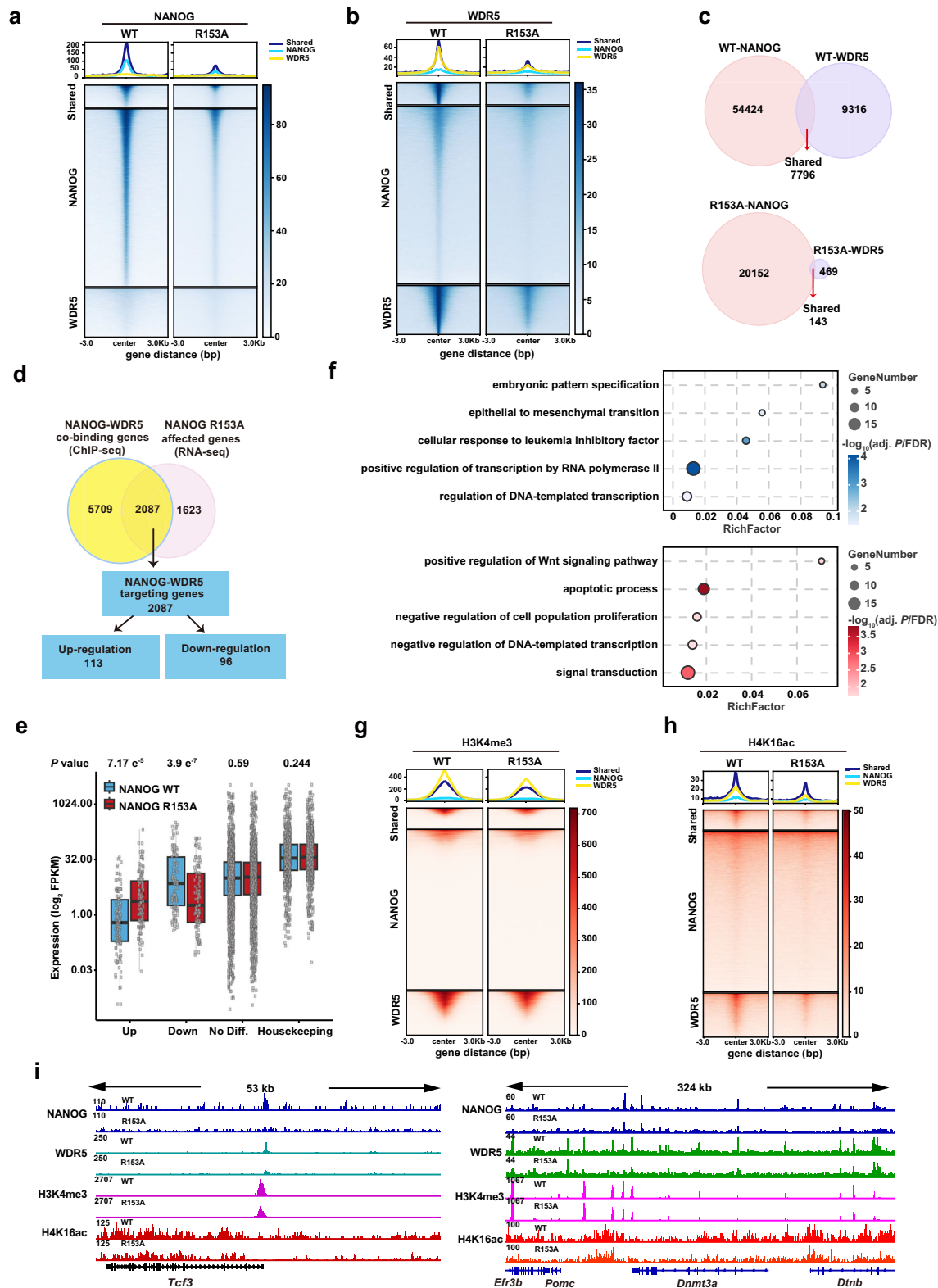
Given that WDR5 is a core component of both the MLL/SET complex, which mediates H3K4 trimethylation (H3K4me3), and the MOF complex, responsible for H4K16 acetylation (H4K16ac), we investigated whether disruption of the WDR5-NANOG interaction affects these epigenetic marks at target loci. ChIP-seq profiling in NANOG<sup>R153A</sup> mESCs revealed global reductions in both H3K4me3 and H4K16ac, with the most marked losses at co-occupied WDR5-NANOG regions (Fig. 5g, h). Representative loci showed context-specific

chromatin remodeling patterns. For example, at the *Tcf3* locus, NANOG, WDR5, and H3K4me3 were co-enriched in wild-type cells but all diminished in the mutant, indicating that the WDR5-NANOG interaction is required to maintain H3K4me3 at this site (Fig. 5i, left). At *Dnmt3a*, NANOG, WDR5, H3K4me3, and H4K16ac were co-localized and reduced in the mutant (Fig. 5i, right), indicating that the WDR5-NANOG interaction contributes to maintaining both activating marks at this promoter. Similar patterns were observed at other pluripotency genes, such as *Nr5a2* and *Esr1b* (Supplementary Fig. 7d).

These genome-wide analyses describe the steady-state chromatin changes associated with disruption of the WDR5-NANOG interaction. To relate these changes to the dynamics of differentiation, we used a time-resolved differentiation assay to place these changes into a temporal framework. NANOG<sup>WT</sup> and NANOG<sup>R153A</sup> ESCs were shifted from 2i/LIF to serum/LIF and harvested at 0, 6, and 24 h. Within the first 6 h after 2i withdrawal, H3K4me3 levels at WDR5-NANOG co-bound pluripotency promoters dropped significantly in R153A cells, and H4K16ac decreased at a subset of the same loci (Supplementary Fig. 8a, b). At this early stage, steady-state mRNA levels showed only modest, gene-specific changes (Supplementary Fig. 8c), whereas a parallel nascent RNA labeling experiment, performed immediately after transfer from 2i/LIF to serum/LIF, already revealed reduced transcription of the same gene set in NANOG<sup>R153A</sup> ESCs (Supplementary Fig. 8d). More uniform down-regulation of bulk mRNA became evident by 24 h (Supplementary Fig. 8c). These kinetics indicate that disruption of WDR5-NANOG condensates first destabilizes activating histone marks and attenuates nascent transcription at pluripotency-associated genes, with loss of steady-state expression arising as a downstream consequence of these epigenetic changes. Thus, the WDR5-NANOG interaction emerges as a critical determinant of active chromatin and transcriptional programs that sustain stem cell identity.

### Targeting WDR5-NANOG suppresses LSC self-renewal

Building on our findings in mESCs, we next examined whether the WDR5-NANOG interaction is also functionally relevant in pathological contexts, particularly in the maintenance of CSCs. Leukemia stem cells represent a prototypical malignant stem cell population, characterized by sustained self-renewal, impaired differentiation, and resistance to chemotherapy. To evaluate the potential involvement of the WDR5-NANOG axis in LSC function, we first analyzed the expression levels of NANOG and WDR5 across human hematopoietic lineages using publicly available single-cell RNA-seq data. Both genes were preferentially expressed in hematopoietic stem and progenitor cells (HSPCs), with significantly lower expression in differentiated subsets (Supplementary Fig. 9a). Utilizing a murine acute myeloid leukemia (AML) model driven by the AML1-ETO9a (AE9a) fusion oncogene<sup>45</sup>, which mimics the human RUNX1::RUNX1T1 translocation and is known to generate a therapy-resistant LSC population, we found that NANOG expression



was upregulated in AE9a HSPCs, while WDR5 levels remained comparable to those in WT HSPCs (Fig. 6a). These observations indicate that the self-renewal ability of AE9a HSPCs may depend on elevated NANOG expression and its interaction with WDR5.

To functionally interrogate this hypothesis, we targeted the WDR5-NANOG axis in AE9a LSCs using C16<sup>46</sup>, a selective small-molecule inhibitor that binds the WIN site of WDR5 (Supplementary

Fig. 9b). Endogenous Co-IP experiments showed that C16 preferentially weakened the WDR5-NANOG interaction, whereas WDR5 complexes with MLL1 or KANSL1 were only modestly affected at the concentrations tested (Supplementary Fig. 9c). We further used revumenib (RE)<sup>47</sup>, a selective menin-MLL1 inhibitor, to differentiate potential effects arising from MLL1-related pathways. In AE9a leukemia cells, C16 treatment significantly reduced colony-forming units (CFUs)

**Fig. 5 | Loss of the WDR5-NANOG interaction compromises histone modifications at promoters of pluripotency-associated genes.** Heatmaps showing the genome-wide ChIP-seq binding profiles (merged from  $n = 2$  independent biological replicates per condition) of NANOG (a) and WDR5 (b) at NANOG-specific, WDR5-specific, and shared binding sites in mESCs expressing NANOG<sup>WT</sup> or NANOG<sup>R153A</sup> ( $\pm 3$  kb from peak center). c Venn diagram summarizing the shared numbers of NANOG and WDR5 ChIP-seq peaks observed in NANOG<sup>WT</sup> and NANOG<sup>R153A</sup> mESCs. d Venn diagram showing the overlap between genes co-bound by NANOG and WDR5 in WT mESCs (identified by ChIP-seq) and genes differentially expressed in NANOG<sup>R153A</sup> mESCs (identified by RNA-seq). e Box plots (related to Fig. 5d) showing the expression levels of WDR5-NANOG target genes in NANOG<sup>WT</sup> and NANOG<sup>R153A</sup> mESCs. Genes were categorized into groups with increased binding ( $n = 113$  genes), decreased binding ( $n = 96$  genes), no significant change ( $n = 1878$  genes), and housekeeping genes ( $n = 811$  genes). Box plots show the median (center line), with

boxes indicating the 25th and 75th percentiles (interquartile range). Whiskers extend to the most extreme data points within  $1.5\times$  the interquartile range. Individual data points are overlaid.  $P$  values were calculated using unpaired two-sided  $t$ -tests. f GO enrichment analysis (related to Fig. 5d) was performed using DAVID. Downregulated and upregulated gene sets were analyzed separately using a one-sided hypergeometric test, with  $P$  values adjusted by the Benjamini-Hochberg method (FDR). Dot size indicates gene number and color indicates  $-\log_{10}$  (adjusted  $P$  value). Heatmaps showing the genome-wide ChIP-seq binding profiles (merged from  $n = 2$  independent biological replicates per condition) of H3K4me3 (g) and H4K16Ac (h) at NANOG-specific, WDR5-specific, and shared binding sites in mESCs expressing NANOG<sup>WT</sup> or NANOG<sup>R153A</sup> ( $\pm 3$  kb from peak center). i Representative genome browser tracks showing ChIP-seq signals for NANOG, WDR5, H3K4me3, and H4K16ac at the *Tcf3* and *Dnmt3a* loci.

and decreased the number of viable AE9a cells by approximately 60% compared to the DMSO control group, whereas RE had minimal impact on either parameter (Fig. 6b). In WT HSPCs, both C16 and RE treatments reduced CFUs by about 15% compared to the DMSO control group. However, RE led to a sharp 75% decline in cell viability, while C16 only caused a modest -10% decrease (Fig. 6b). Fluorescence-activated cell sorting (FACS) analysis further revealed that C16 treatment almost completely depleted the LSC population, while LSCs in the DMSO and RE groups remained at 6%. The flow cytometry gating strategies are shown in Supplementary Fig. 10a, b. Additionally, C16 treatment promoted the differentiation of AE9a leukemia cells into mature myeloid cells (Fig. 6c). Taken together, these results suggest that targeting the WDR5-NANOG axis specifically inhibits the self-renewal of LSCs in the AE9a leukemia model in vitro.

To gain insights into the molecular mechanisms, we performed RNA-seq analysis on C16- or RE-treated AE9a and WT c-Kit<sup>+</sup> cells. Among all groups, C16-treated AE9a cells exhibited the most extensive transcriptional alterations (Fig. 6d, Supplementary Fig. 10c). A total of 3,323 genes were downregulated in the C16-treated AE9a group, among which 2,941 were specifically downregulated in AE9a cells compared to C16-treated WT cells (Fig. 6e). In contrast, only 259 genes were downregulated in RE-treated AE9a cells (Supplementary Fig. 10d). The number of upregulated genes in these groups was less dramatically different relative to WT cells, with 846 genes upregulated in C16-treated AE9a cells and 478 genes upregulated in RE-treated AE9a cells (Supplementary Fig. 10e, f). Next, we performed GO analysis to examine the functional impact of these transcriptional changes. The downregulated genes were associated with stemness-related processes, including embryonic hematopoiesis, stem cell proliferation, and the Notch signaling pathway, while the upregulated genes were predominantly involved in differentiation processes, such as cell differentiation and the Wnt signaling pathway (Fig. 6f). These results suggest that C16 exerts its unique effects on AE9a LSCs primarily through the suppression of transcriptional programs essential for stem cell maintenance. We further evaluated the in vivo effects of C16 treatment on AE9a LSCs using a retrovirus-transformed AE9a mouse leukemia model (Fig. 6g). Consistent with the in vitro results, C16-treated mice showed a ~50% reduction in the populations of lineage Sca-1<sup>+</sup>c-Kit<sup>+</sup> (LSK) cells, long-term hematopoietic stem cells (LT-HSCs), and multi-potent progenitor (MPP) cells compared to the DMSO control group, while RE treatment had a minimal effect on these populations in AE9a recipient mice (Fig. 6h and Supplementary Fig. 10g). Analysis of downstream progenitor cells revealed that RE treatment significantly expanded the populations of common myeloid progenitors (CMP) and granulocyte-monocyte progenitors (GMP), while C16 treatment showed comparable populations of these cells to the DMSO group (Supplementary Fig. 10g, h). Together, these findings indicate that C16 selectively impairs the expansion of stem cells in the AE9a mouse leukemia

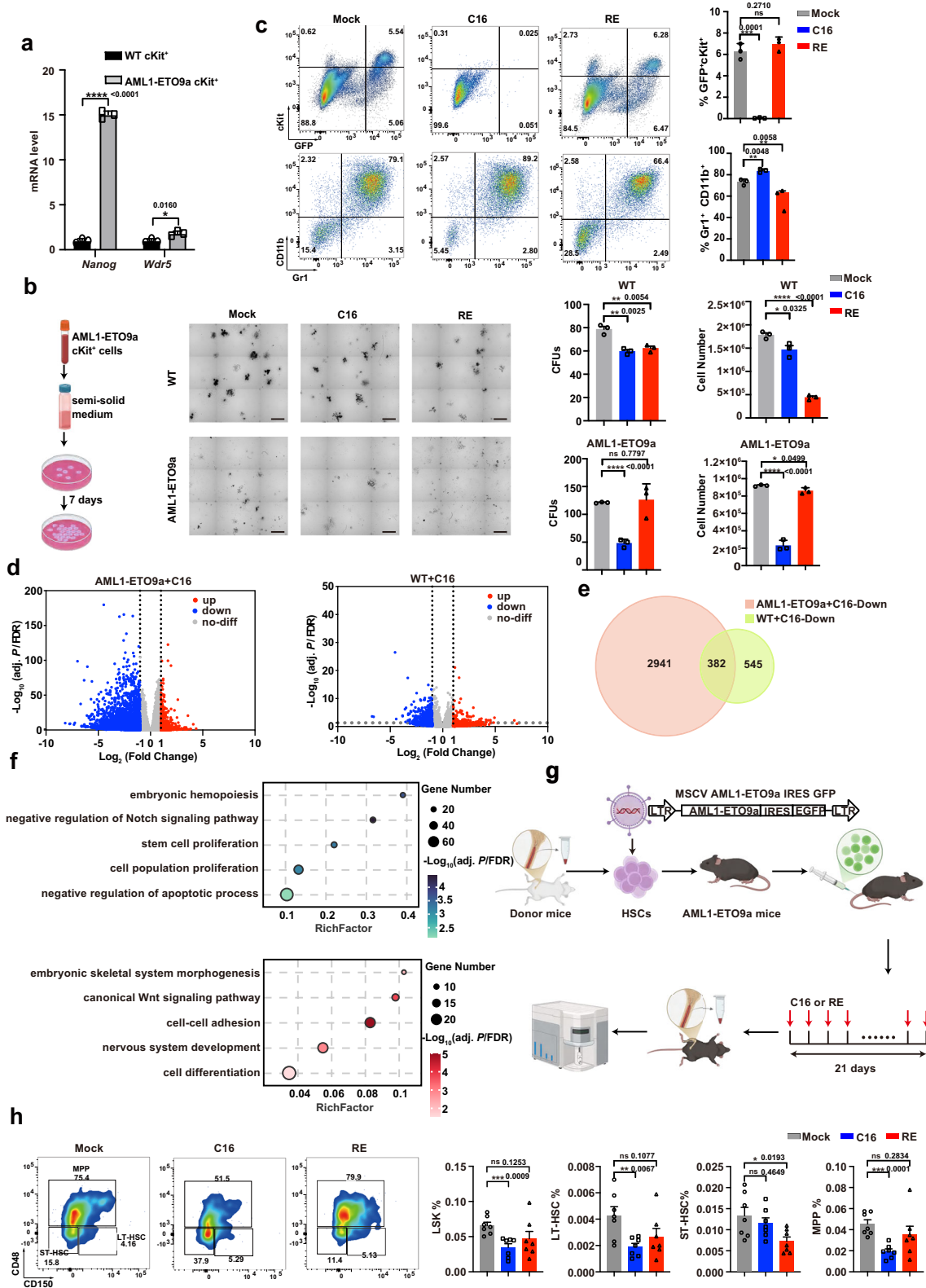
model, highlighting the therapeutic potential of targeting the WDR5-NANOG axis to eliminate leukemia stem cells.

## Discussion

Stem cell pluripotency is maintained through the coordinated and spatially organized interplay between transcription factors and chromatin regulators. Recent evidence indicates that core pluripotency factors such as OCT4 and TAZ can undergo LLPS to assemble transcriptional condensates, enriching coactivators like BRD4 and p300 at super-enhancer regions and driving robust gene activation<sup>17,48</sup>. In these previously described mechanisms, LLPS is predominantly driven by transcription factors themselves, with chromatin-associated proteins typically serving as passive interactors. However, whether chromatin regulators can actively reshape the condensate properties of transcription factors has remained largely unexplored.

Here, we demonstrate that the chromatin adapter WDR5 actively remodels the phase separation behavior of the pluripotency factor NANOG. Through a direct, noncanonical interaction involving the NANOG homeodomain, WDR5 transforms NANOG assemblies from aggregation-prone states into dynamic, liquid-like condensates. This remodeling enables efficient recruitment of histone-modifying complexes such as MLL and MOF to pluripotency-associated gene promoters. Unlike canonical WDR5 interactions, which usually involve short WIN or WBM peptide motifs, the WDR5-NANOG interaction utilizes an extended interface spanning both structured and intrinsically disordered regions. Importantly, this binding mode is unique to NANOG among homeodomain-containing transcription factors, highlighting its biochemical specificity.

Our findings broaden current views of transcriptional regulation by LLPS. Recent work has shown that transcription factors can adopt a spectrum of material states, extending beyond classical liquid-like condensates to less dynamic or amorphous assemblies under defined conditions. For example, SOX2 droplets formed in vitro gradually mature into amorphous aggregates rather than remaining spherical<sup>49</sup>. MYC undergoes stress-responsive multimerization<sup>50</sup> and displays sequence-dependent phase separation in which a negatively charged region controls condensate formation and irreversible aggregation<sup>51</sup>. Together with our observation that NANOG forms  $\beta$ -sheet-enriched, irregular aggregates that are remodeled by WDR5, these findings support a view in which transcription factor condensates can exist in multiple material states and that their material properties are adjustable. In this context, WDR5 is not merely a passive binding partner, but an active modulator that structurally remodels NANOG condensates and couples them to epigenetic activation machinery. Similar protein-protein remodeling has been observed previously—for instance, Kap $\beta$ 2 altering the phase properties of FUS<sup>52</sup> and HSP70 modulating TDP-43 condensates to prevent aggregation<sup>53</sup>. Our study now provides a clear example of how a chromatin-associated factor



can directly regulate the phase behavior of an aggregation-prone transcription factor to influence cell fate decisions.

Through integrated ChIP-seq, time-resolved ChIP-qPCR, nascent RNA and RNA-seq analyses, we demonstrate that WDR5-NANOG interactions facilitate genome-wide chromatin binding and epigenetic activation essential for maintaining pluripotency. Disruption of the WDR5-NANOG interaction in NANOG<sup>R153A</sup>-expressing mESCs reduces chromatin occupancy at shared binding sites and diminishes

H3K4me3 and H4K16ac at pluripotency promoters, with loss of these activating marks and reduced nascent transcription preceding broader decreases in steady-state mRNA levels. While some transcriptional changes may reflect secondary effects due to loss of pluripotency, the subset of genes with coordinated changes in both WDR5-NANOG binding and gene expression provides strong evidence for a direct regulatory role of these condensates in sustaining pluripotency-associated transcriptional networks.

**Fig. 6 | Targeting the WDR5-NANOG axis suppresses the self-renewal of AML1-ETO9a (AE9a) leukemia stem cells.** **a** mRNA expression levels of *Nanog* and *Wdr5* in WT and AE9a hematopoietic stem and progenitor cells (HSPCs). Data are mean  $\pm$  SD from three independent replicates. \* $P < 0.05$ , \*\*\*\* $P < 0.0001$  by unpaired two-sided t-test. **b** Representative images and quantification of colony-forming units (CFUs) generated by WT and AE9a c-Kit<sup>+</sup> cells cultured in methylcellulose following treatment with DMSO (Mock), C16 (2  $\mu$ M), or Revumenib (2  $\mu$ M). Data are mean  $\pm$  SD from three independent replicates. ns:  $P > 0.05$ , \* $P < 0.05$ , \*\* $P < 0.01$ , \*\*\*\* $P < 0.0001$  by unpaired two-sided t-test. Scale bars, 2 mm. **c** Flow cytometry analysis (FACS) of stem cell populations in AE9a cells treated with DMSO (Mock), C16 (2  $\mu$ M), or Revumenib (2  $\mu$ M). Data are mean  $\pm$  SD from three independent replicates. ns:  $P > 0.05$ , \*\* $P < 0.01$ , \*\*\* $P < 0.001$  by unpaired two-sided t-test. **d** Volcano plots of differentially expressed genes (DEGs) in C16-treated AE9a and WT c-Kit<sup>+</sup> cells compared to DMSO controls, analyzed with DESeq2.  $P$  values were calculated using the two-sided Wald test and adjusted by Benjamini-Hochberg

method (FDR). Dashed lines indicate the thresholds  $|\log_2[\text{fold change}]| \geq 1$  and  $\text{FDR} < 0.05$ . RNA-seq was performed using three biological replicates. **e** Venn diagram showing the overlap of downregulated genes between C16-treated AE9a and WT c-Kit<sup>+</sup> cells. **f** GO enrichment analysis of downregulated and upregulated genes in C16-treated AE9a cells relative to DMSO-treated controls, analyzed with DAVID. Downregulated and upregulated gene sets were analyzed separately using a one-sided hypergeometric test, and  $P$  values were adjusted with the Benjamini-Hochberg method (FDR). Dot size indicates gene number and color indicates  $-\log_{10}$  (adjusted  $P$  value). **g** Schematic of the C16 in vivo inhibition assay. **h** FACS analysis of stem cell populations in AE9a recipient mice following 21-day treatment with C16 or Revumenib. Data represent mean  $\pm$  SEM ( $n = 7$  mice). ns:  $P > 0.05$ , \* $P < 0.05$ , \*\* $P < 0.01$ , \*\*\* $P < 0.001$ , \*\*\*\* $P < 0.0001$  by unpaired two-sided t-test. Source data are provided as a Source Data file. Figure 6b, g: Created in BioRender. Shi, Y. (2026) <https://BioRender.com/h76z570>.

Moreover, disruption of the WDR5-NANOG interaction impairs leukemia stem cell self-renewal. Notably, treatment with the WDR5 inhibitor C16 in LSCs induces phenotypic and transcriptional changes similar to those observed in mESCs expressing NANOG<sup>R153A</sup>, suggesting a conserved functional axis in oncogenic and developmental contexts. These observations broaden the implications of WDR5-NANOG condensates from developmental biology into cancer, providing a new conceptual framework for targeting LLPS-driven transcriptional mechanisms in disease.

Collectively, our study establishes a direct link between structural remodeling of transcription factor condensates and precise epigenetic regulation of stem cell identity (Fig. 7). By demonstrating how WDR5 actively modulates NANOG condensate dynamics to promote transcriptional competency at pluripotency-associated loci, we identify a fundamental regulatory logic that integrates phase separation with chromatin-based mechanisms. This concept likely applies broadly across transcriptional hubs and suggests promising avenues for therapeutic interventions targeting LLPS-associated pathways in stem cell disorders and malignancies.

## Methods

### Cell lines

*Wdr5* C-terminal 3 $\times$  Flag and *Nanog* R153A knock-in cell lines were generated by the CRISPR-Cas9 method. First, AG-haESC were transfected with a plasmid expressing Cas9/sgRNA along with a recombination donor DNA flanked by homology arms targeting either the *Wdr5* C-terminal or the R153 site of *Nanog*. Three days after transfection, mCherry-positive cells were isolated by FACS, expanded, and validated via immunoblotting and Sanger sequencing. The sgRNA sequences for *Wdr5*-3 $\times$ Flag and *Nanog* R153A knock-in are 5'-GAA-GAGTACTGCTAAGTCC-3' and 5'-ACCAAAGGATGAAGTGCAAG-3', respectively.

### Cell culture

HEK293T and HEK293A cells were cultured in high-glucose DMEM (Gibco, 11995065) supplemented with L-glutamine and sodium pyruvate and 10% fetal bovine serum (ExCell Bio, FSP500) at 37 °C and 5% CO<sub>2</sub>.

For the maintenance of naive pluripotency under 2i/LIF conditions, mouse embryonic stem cells (mESCs) were cultured on dishes coated with 0.1% gelatin, using a serum-free N2B27 medium composed of equal parts DMEM/F12 and Neurobasal media. This base was supplemented with 1  $\times$  B27, 1  $\times$  N2, 2 mM L-glutamine, 50 U/ml penicillin-streptomycin, and 0.1 mM 2-mercaptoethanol. To sustain the naive state, the medium also included 3  $\mu$ M CHIR99021 (a GSK3 $\beta$  inhibitor), 1  $\mu$ M PDO325901 (a MEK inhibitor), and recombinant leukemia inhibitory factor (LIF).

For downstream applications, mESCs initially grown in 2i/LIF were passaged and transferred to serum/LIF medium, with a medium

replacement 24 h post-transfer. Cells were collected 48 h later for RNA-seq and ChIP-seq analyses.

For serum/LIF culture, mESCs were maintained on 0.1% gelatin-coated plates in conventional ESC medium consisting of high-glucose DMEM supplemented with 15% fetal bovine serum (FBS), 100  $\mu$ M non-essential amino acids (NEAA), 1% nucleoside mix, 2 mM L-glutamine, 50 U/ml penicillin-streptomycin, 0.1 mM 2-mercaptoethanol, and in-house produced recombinant LIF, which was functionally validated for supporting self-renewal. Cultures were maintained at 37 °C in a humidified atmosphere containing 5% CO<sub>2</sub>.

Mouse cKit<sup>+</sup> cells were cultured in SFEM medium (STEMCELL, Cat #09650) supplemented with 100 ng/mL murine SCF (R&D), 20 ng/mL murine IL-3 (R&D), and 20 ng/mL murine IL-6 (R&D). For RNA-seq analysis, cKit<sup>+</sup> cells were treated for 72 h with either DMSO, 5  $\mu$ M C16 (WDR5-IN-1, HY-133121, MedChemExpress) or 10  $\mu$ M Revumenib (HY-136175, MedChemExpress) for 72 h.

### Protein expression and purification

*Mus musculus Nanog* and *Wdr5* fragments were amplified by G5 High-Fidelity DNA Polymerases (EnzyArtisan, China). Full-length WDR5 and NANOG, as well as their truncations or mutants, were cloned into a modified pET28b vector with an N-terminal 6 $\times$ His-Sumo tag using One-Tube Cloning Kit (EnzyArtisan, China). The plasmids were then extracted with the SPARKeasy Superpure Mini Plasmid Kit (Shandong Sparkjade Biotechnology Co., Ltd.) and transformed into *Escherichia coli* BL21(DE3) competent cells (WEIDI bio, China, EC1002).

For WDR5 and soluble NANOG fragments, proteins were overexpressed with induction by 0.2 mM isopropyl  $\beta$ -D-1-thiogalactopyranoside (IPTG) for 16–18 h at 18 °C. Harvested cells were resuspended in lysis buffer containing 50 mM Tris-HCl, pH 8.0, 400–800 mM NaCl, 10% glycerol, 2 mM 2-mercaptoethanol, and protease inhibitor cocktail. The cells were broken by sonication on ice and then centrifuged at 20,000  $\times g$  for 40 min. The supernatant was incubated with Ni-NTA beads (Qiagen, USA) for 2 h at 4 °C, and the tag-free proteins were then eluted by on-beads digestion with ULP1 protease (for pET28b-Sumo vectors) added at a molar ratio of 1:200. Eluted proteins were further purified by size-exclusion chromatography (SEC) on Hiload Superdex 75 or Hiload Superdex 200 columns in the buffer of 25 mM Tris-HCl, pH 8.0, and 150–300 mM NaCl. Purified proteins were concentrated and stored at –80 °C.

Full-length NANOG was expressed by induction with 1 mM IPTG at 37 °C for 3–4 h and accumulated predominantly in inclusion bodies. Bacterial pellets were resuspended in denaturing buffer (50 mM Tris-HCl, pH 8.0, 800 mM NaCl, 8 M urea) containing protease inhibitors, lysed by sonication, and centrifuged to remove insoluble debris. The supernatant was applied to Ni-NTA resin in the same denaturing buffer, washed, and eluted with imidazole. Denatured NANOG was then refolded by stepwise dialysis into buffers with decreasing urea concentrations (4 M, 2 M, and 0 M) and finally into 50 mM Tris-HCl pH 8.0,

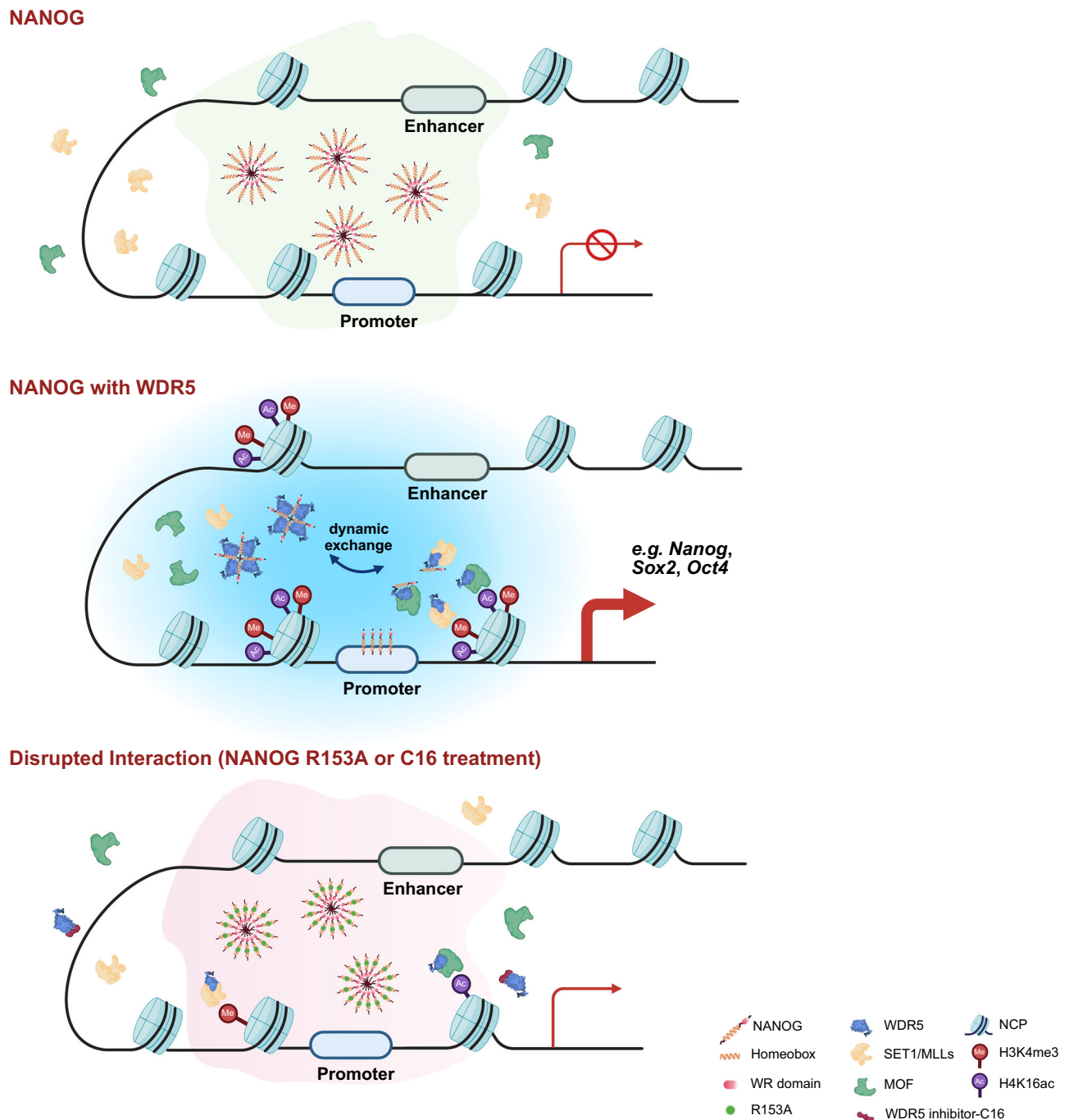


**Fig. 7 | Schematic model of LLPS-mediated WDR5-NANOG interaction in transcriptional activation and pluripotency maintenance.** In the absence of WDR5, NANOG tends to form irregular aggregates that are less competent for productive chromatin engagement and cofactor recruitment, resulting in reduced activation of pluripotency-associated genes. Upon WDR5 binding, NANOG is remodeled into dynamic, liquid-like condensates that can co-enrich histone-modifying complexes

(e.g., SET1/MLL and MOF), supporting H3K4me3 and H4K16ac at target loci and thereby promoting gene activation. Disruption of the WDR5-NANOG interaction by either the R153A mutation or C16 treatment shifts NANOG toward a less dynamic, aggregated state, thereby impairing transcriptional activation of pluripotency-associated genes. Created in BioRender. Shi, Y. (2025) <https://BioRender.com/r4b9esd>.

400 mM NaCl, 1 mM DTT, 10% glycerol. Precipitates were removed by centrifugation, the SUMO tag was cleaved with ULP1 where applicable, and refolded protein was further purified by SEC in 25 mM Tris-HCl pH 8.0, 300 mM NaCl and concentrated for downstream assays.

For NMR, uniformly  $^{15}\text{N}$ ,  $^{15}\text{N}/^{13}\text{C}$  and  $^{15}\text{N}/^{13}\text{C}/^2\text{H}$ -labeled proteins were produced in M9 minimal medium containing  $^{15}\text{NH}_4\text{Cl}$  (and  $^{13}\text{C}$ -glucose and  $\text{D}_2\text{O}$  where appropriate) and purified following the same protocol. The protein concentration was measured by UV

absorbance at 280 nm or a BCA Protein Assay Kit (TIANGEN, PA115-01, China).

#### GST pull down

For pull-down assays, 100  $\mu\text{g}$  of GST-tagged WDR5 and 100  $\mu\text{g}$  NANOG full-length proteins were mixed with 10  $\mu\text{L}$  of glutathione Sepharose 4B beads in 100  $\mu\text{L}$  of binding buffer (25 mM Tris-HCl, pH 8.0, 150 mM NaCl, and 2 mM DTT). 10  $\mu\text{L}$  reaction mixtures were taken out as input

controls. After incubation at the indicated temperature for 3 h, the beads were washed four times with 500  $\mu$ L of the binding buffer. The bound samples were eluted with 25  $\mu$ L elution buffer (15 mM reduced glutathione, 25 mM Tris-HCl, pH 8.0, 150 mM NaCl, and 2 mM DTT). The input and eluted samples were analyzed by SDS-PAGE.

### Fluorescence polarization assay

NANOG HD<sup>WT</sup> and NANOG HD<sup>R153A</sup> proteins were serially diluted in buffer containing 25 mM HEPES, pH 7.8, 150 mM NaCl, 10% glycerol. An equal volume of 5'-FAM-labeled Tcf3 DNA (acctgttaatgggagcgc, synthesized by GenScript Biotech Corporation) was added to each tube to reach a final concentration of 25 nM. The reaction mixtures were incubated on ice for 30 min in the dark and transferred to a 384-well plate. Fluorescence polarization values were measured using a Synergy Neo Multi-Mode Reader (Bio-Tek, USA) at an excitation wavelength of 485 nm and an emission wavelength of 528 nm.

### Electrophoretic mobility shift assay

NANOG HD<sup>WT</sup>, NANOG HD<sup>R153A</sup> and WDR5 proteins were serially diluted in either a low-salt binding buffer (10 mM HEPES pH 7.8, 50 mM KCl, 10 mM NaCl, 10% glycerol) or a physiological-salt buffer (25 mM HEPES pH 7.8, 150 mM NaCl, 10% glycerol). For NANOG-DNA binding assays, an equal volume of 5'-FAM-labeled Tcf3 DNA (acctgttaatgggagcgc; synthesized by GenScript Biotech Corporation) was added to each tube. For competition assays, NANOG HD and 5'-FAM-labeled Tcf3 DNA were pre-incubated in the low-salt buffer, and increasing amounts of WDR5 were then added while keeping NANOG and DNA concentrations constant. After incubation on ice for 30 min in the dark, the reaction mixtures were loaded onto 6% native polyacrylamide gels and separated by electrophoresis. Gels were imaged using an FLA-9000 scanner (STARION).

### Co-immunoprecipitation

HEK293T cells were harvested and washed with PBS buffer. The cells were suspended in 500  $\mu$ L lysis buffer (25 mM Tris-HCl, pH 8.0, 150 mM NaCl), and then broken by sonication. The cell lysates were centrifuged for 15 min at 12,000  $\times g$  at 4 °C. The supernatant was mixed with 10  $\mu$ L Anti-DYKDDDDK Affinity Beads (Smart-Lifesciences, China, SA042025) followed by incubation at 4 °C for 3 h. Beads were washed three times with 1 ml wash buffer (25 mM Tris-HCl, pH 8.0, 150 mM NaCl, 0.1% NP-40), and the bound samples were eluted by 40  $\mu$ L 1  $\times$  SDS loading buffer. Immunoprecipitation was conducted using anti-Flag (ABclonal, AE024, 1:2000) and anti-HA (Cell Signaling, 3724 s, 1:1000).

For endogenous co-immunoprecipitation, WDR5-Flag knock-in mESCs were harvested and washed with PBS. The cells were suspended in 200  $\mu$ L lysis buffer (25 mM Tris-HCl, pH 8.0, 150 mM NaCl, 1% NP-40) and lysed by sonication. After centrifuging at 12,000  $\times g$  for 15 min at 4 °C, the supernatants were collected and treated with 0  $\mu$ M, 5  $\mu$ M or 20  $\mu$ M Cl<sub>16</sub>, respectively. Each sample was then incubated with 10  $\mu$ L of Anti-DYKDDDDK Affinity Beads (Smart-Lifesciences, China, SA042025) for 3 h at 4 °C with gentle mixing. Beads were washed three times with 200  $\mu$ L lysis buffer, and bound proteins were eluted with 30  $\mu$ L 1  $\times$  SDS loading buffer. Immunoblotting was performed using the following antibodies: anti-Flag (ABclonal, AE024, 1:2000), anti-MLL1 (Cell Signaling Technology, 14197S, 1:1000), anti-NANOG (Cell Signaling Technology, 8822S, 1:1000) and anti-KANSL1 (Aviva Systems Biology, ARP55255\_P050, 1:500).

### Isothermal titration calorimetry (ITC)

ITC experiments were performed on a MicroCal ITC200 system (GE Healthcare, USA) at 20 °C. Before measurement, proteins were dialyzed into the same buffer (25 mM Tris-HCl, pH 8.0, 150 mM NaCl). For ITC experiments, WDR5 at 1.0 mM in the syringe was titrated into NANOG proteins (including truncations and mutation proteins) at

0.1 mM in the sample cell. Each titration consisted of 20 successive injections. The titration curves were processed using the Origin 7.0 software program (OriginLab) according to the "one binding site" fitting model. Each titration was repeated twice, and one representative plot was shown in the paper. The dissociation constants<sup>54</sup>, enthalpy changes ( $\Delta H$ ), and fitting errors were derived from the representative ITC plot.

### Crystallization and structural determination

NANOG HD<sup>R100A</sup>-WDR5 complex was concentrated to 15 mg/mL for crystallization, and the crystal was obtained by the sitting-drop vapor diffusion method at 4 °C by mixing 0.3  $\mu$ L protein-protein complex solution and 0.3  $\mu$ L crystal solution. The complex was crystallized in a solution composed of 100 mM BIS-TRIS pH 6.5, 2.0 M Ammonium sulfate. The crystal was cryoprotected in the same reservoir solution supplemented with 20% glycerol. The datasets were collected at the beamline BL19U1 of the Shanghai Synchrotron Radiation Facility and processed using HKL2000<sup>55</sup>. The structures were solved by molecular replacement in PHASER<sup>56</sup> by using the following template models: 2GNQ<sup>57</sup> and 2VI6<sup>40</sup>. The MR models were then refined by using PHENIX<sup>58</sup> suite with manual building in COOT<sup>59</sup>, and the structural details were analyzed by PyMol (1.5.0).

### Phase separation assays in vitro and in vivo

For in vitro experiments, purified GFP-NANOG<sup>WT</sup>, GFP-NANOG<sup>R153A</sup>, WDR5<sub>1-334</sub>-RFP proteins were dialyzed into the protein buffer (25 mM Tris-HCl, pH 8.0, 150 mM NaCl). Proteins and AMCA-labeled Tcf3 DNA (acctgttaatgggagcgc, synthesized by GENERAL BIOL, Chuzhou, China) were then diluted to the desired concentration in the droplet formation buffer (25 mM Tris-HCl, pH 8.0, 150 mM NaCl, 5% PEG8000). For droplet visualization, 3–6  $\mu$ L of the protein solution was deposited onto a microscope slide. Fluorescent images were acquired using a Zeiss LSM 710 microscope.

For in vivo 293A imaging, 1  $\times 10^5$  cells were grown on a cell culture plate (Cellvis, D29-14-1.5-N). Transfection was performed 18 h after plating when cell density reached ~30–40% confluency. For each well, 1  $\mu$ g of each plasmid was transfected using 2  $\mu$ L Lipo293<sup>TM</sup> transfection reagent (Beyotime, China, C0521) diluted in 125  $\mu$ L opti-MEM (Gibco, 31985). Cells were cultured for ~48 h post-transfection, and then incubated with Hoechst 33342 (Beyotime, China, C1022) for 5 min. After washing twice with 1  $\times$  PBS, fluorescent images were captured using a confocal laser scanning microscopy Olympus SpinSR 10 under 100 $\times$  oil immersion objective. Excitation lasers at 405 nm, 488 nm, and 561 nm were used to visualize Hoechst, GFP and RFP signals, respectively.

### Fluorescence recovery after photobleaching (FRAP) measurements

Fluorescence recovery after photobleaching (FRAP) experiments were performed on in vitro droplets using a Zeiss LSM 710 confocal microscope equipped with 488 nm and 561 nm laser lines and a 63 $\times$ /1.40 NA oil-immersion objective. Defined regions within individual droplets were photobleached for 100 iterations. After bleaching, fluorescence intensities in the bleached area were recorded every 10 s. The raw data ( $n=15$ ) were processed and analyzed by GraphPad Prism 9.

For live-cell FRAP, 293A cells expressing GFP-NANOG and WDR5-RFP were imaged on a Leica TCS SP8 confocal microscope. Puncta were photobleached with a 488 nm laser (laser bleach 300 iterations; image acquisition interval, 5 s). The raw data ( $n=20$ ) were processed and analyzed by GraphPad Prism 9.

### NMR spectroscopy

The NMR experiments were carried out at 25 °C on Agilent DD2 600 MHz or 800 MHz spectrometers equipped with a cryogenic

probe. Chemical shifts were referenced to external DSS. For the assignment of backbone resonances of WDR5, the U- $^{13}\text{C}$ ,  $^{15}\text{N}$  NMR samples were prepared in NMR buffer containing 40 mM HEPES (pH 7.5), 150 mM NaCl, 1× Protease Inhibitor Cocktail (MedChemExpress, HY-K0010), 1 mM PMSF, 0.03%  $\text{NaN}_3$ , 3 mM DTT, and 90%  $\text{H}_2\text{O}$  / 10%  $\text{D}_2\text{O}$ . The conventional TROSY versions of standard triple resonance experiments were acquired, including HNCO, HN(CA)CO, HNCA, HN(CO)CA, HN(COCA)CB and HNCACB<sup>60</sup>. In addition, a nuclear overhauser effect (NOE) mixing time of 150 ms was recorded for a 3D  $^{15}\text{N}$ -edited NOESY-HSQC experiment to validate backbone assignments. Spectra were processed with NMRPipe<sup>61</sup> and analyzed with NMRFAM-SPARKY<sup>62</sup>.

For the assignment of backbone resonances of NANOG HD, the U- $^{13}\text{C}$ ,  $^{15}\text{N}$  NMR samples were prepared in NMR buffer containing 25 mM HEPES (pH 7.0), 300 mM NaCl, 1× Protease Inhibitor Cocktail (MedChemExpress, HY-K0010), 0.03%  $\text{NaN}_3$  (w/v), 3 mM DTT, and 90%  $\text{H}_2\text{O}$ /10%  $\text{D}_2\text{O}$ . NMR spectra were collected at 25 °C on an Agilent DD2 700 MHz spectrometer equipped with a HCN z-gradient room temperature probe. The backbone assignments were obtained using HNCO, HNCACO, CBCA(CO)NH, HNCACB, HNCA, HN(CO)CA and  $^{15}\text{N}$ -edited NOESY-HSQC spectra. All 3D spectra employed a non-uniform sampling scheme in the indirect dimensions and were reconstructed by multi-dimensional decomposition software MddNMR<sup>63,64</sup>, interfaced with NMRPipe.

To investigate the interaction between WDR5 and NANOG HD, 0.5 mM U- $^{15}\text{N}$  WDR5 was titrated with unlabeled NANOG HD at a 1:3 molar ratio or 0.5 mM U- $^{15}\text{N}$  NANOG HD was titrated with unlabeled WDR5 at a 1:1 molar ratio in a buffer containing 25 mM HEPES (pH 7.5), 300 mM NaCl, 3 mM DTT, 1× Protease Inhibitor Cocktail (MedChemExpress, HY-K0010), 0.03%  $\text{NaN}_3$  and 10%  $\text{D}_2\text{O}$ . The 2D  $^1\text{H}$ - $^{15}\text{N}$  TROSY spectra were recorded at 25 °C on an Agilent DD2 700 MHz spectrometer equipped with a HCN z-gradient room temperature probe.

### RNA-seq

Total RNA was extracted using TRIzol reagent (Sigma-Aldrich) according to the manufacturer's instructions. RNA-seq libraries were prepared with the NuGEN RNA-seq kit (#0348–32) and sequenced on the Illumina HiSeq 4000 platform to generate paired-end reads with a length of 150 nucleotides.

### ChIP-seq and ChIP-qPCR

ChIP-seq and Spike-in ChIP samples were prepared using the SimpleChIP Enzymatic Chromatin IP Kit (Cell Signaling Technology, #9005) following the manufacturer's protocol. Briefly,  $4 \times 10^6$  mESCs were fixed in 1% formaldehyde for 10 min at room temperature and quenched with 125 mM glycine for 5 min. Cells were rinsed three times with ice-cold PBS and stored at -80 °C. For chromatin fragmentation, fixed cells were lysed, and nuclei were digested with micrococcal nuclease (MNase) to obtain mono-nucleosomal fragments. The reaction was stopped with EDTA, and the nuclei were collected by centrifugation. Chromatin extracts were incubated overnight at 4 °C with rotation with the following primary antibodies: anti-NANOG (Bethyl Laboratories, A300-397A, 1:100), anti-H3K4me3 (Cell Signaling Technology, #9751S, 1:100), anti-H4K16ac (Abcam, ab109463, 1:100), or anti-FLAG (Sigma-Aldrich, F1804, 1:100). Immunoprecipitated complexes were captured using Protein G magnetic beads for 2 h at 4 °C. After a series of low-salt and high-salt washes, the chromatin was eluted and reverse-crosslinked at 65 °C in the presence of Proteinase K and NaCl. Purified ChIP DNA was used for library construction using the NEBNext Ultra II DNA Library Prep Kit (E7103S). For quantitative normalization, a calibrated amount of Spike-in DNA was introduced into each sample during the library preparation stage. Libraries were sequenced on an Illumina platform with paired-end 150-bp reads.

ChIP for qPCR analysis was performed using the same cross-linking, chromatin preparation, and immunoprecipitation procedures

described above for ChIP-seq, following the manufacturer's instructions for the SimpleChIP Enzymatic Chromatin IP Kit (Cell Signaling Technology). Immunoprecipitated chromatin and 1.25% input DNA were analyzed by quantitative PCR using SYBR Green Master Mix (Vazyme) on an Applied Biosystems QuantStudio real-time PCR system. Primer sequences targeting the promoters of *Nanog*, *Nr5a2*, *Klf4*, *Tbx3*, and *Dnmt3a* are listed in source data. ChIP-qPCR enrichment was calculated as percent input, and data are presented as mean  $\pm$  SD from three independent replicates.

### Embryoid body (EB) differentiation

To induce EB formation, ESCs were dissociated into single cells and seeded as 30  $\mu\text{L}$  hanging drops containing approximately 1000 cells per drop in ESC medium lacking leukemia inhibitory factor (LIF) to allow spontaneous differentiation. The hanging drops were incubated for 4 days under standard culture conditions (37 °C, 5%  $\text{CO}_2$ ), after which the formed EBs were collected for RT-qPCR analysis.

### Thioflavin T assay

To monitor  $\beta$ -sheet-enriched protein assemblies, we utilized the Thioflavin T (ThT) assay. ThT is a fluorescent dye whose emission increases upon binding to  $\beta$ -sheet-rich structures, thereby reporting on the aggregation state of NANOG. A 1 mM Thioflavin T (ThT, MedChemExpress, HY-DO218) stock solution was prepared in 100% DMSO. The stock was diluted with PBS (pH 7.4) to achieve a final ThT concentration of 20  $\mu\text{M}$  in each well. During the assay, the concentrations of full-length NANOG<sup>WT</sup> and NANOG<sup>W5A</sup> were maintained at 5  $\mu\text{M}$ . Full-length WDR5<sup>WT</sup> or WDR5<sup>F133A</sup> was added at a 2:1 molar ratio relative to NANOG. The reaction mixtures were thoroughly mixed by pipetting up and down. ThT fluorescence was measured in 30  $\mu\text{L}$  reactions using 384-well plates on a SynergyNeo Multi-Mode Reader (Bio-Tek) with excitation and emission wavelengths set at 450 nm and 488 nm, respectively. All experiments were performed in triplicate.

### Immunofluorescence

Immunofluorescence was performed as previously described<sup>65</sup>. The following primary antibodies were applied: anti-FLAG (M2) (Sigma-Aldrich, F1804), anti-NANOG (Cell Signaling Technology, 8822S). Images were acquired using a Leica TCS SP8 confocal laser microscopy system.

### Nascent RNA capture

The nascent RNA synthesis was detected using a STAR-Click Nascent RNA Capture Prep Kit (Foreverstar Biotech, Beijing, China) according to the manufacturer's instructions. Briefly, cells were incubated with 1  $\mu\text{M}$  5-ethynyl uridine (EU), an alkyne-modified nucleoside, for 30 min. Total RNA labeled with EU was then isolated and subjected to a copper-catalyzed click reaction with an azide-modified biotin. This reaction introduced a biotin tag, enabling the capture of nascent RNA transcripts using streptavidin magnetic beads. The captured transcripts were immediately reverse transcribed using TransScript First-Strand cDNA Synthesis SuperMix kit (TransGen Biotech, China) and followed by qPCR analysis. Primer sequences targeting the genes of *Nanog*, *Nr5a2*, *Klf4*, *Tbx3*, and *Dnmt3a* are listed in source data.

### Data analyses

RNA-seq reads were aligned to the mouse genome (mm9) using STAR (v2.7.6a) with default parameters to ensure accurate mapping. Gene-level read counts were used for differential expression analysis with DESeq2. *P* values were calculated using the two-sided Wald test and adjusted by the Benjamini-Hochberg method (FDR). Differentially expressed genes (DEGs) were identified as those with  $|\log_2[\text{fold change}]| \geq 1$  and  $\text{FDR} < 0.05$ . Gene Ontology (GO) analysis was performed using the DAVID platform 6.8 (<https://david.ncifcrf.gov/>). Upregulated and downregulated gene sets were analyzed separately.

GO terms were selected according to adjusted *P* values (Benjamini-Hochberg FDR < 0.05). *P* values were derived from one-sided Fisher's exact test.

ChIP-seq reads were processed using Trim Galore (v0.6.3) for adapter removal and quality filtering, followed by alignment to the mm9 mouse genome with Bowtie2 (v2.3.4). The aligned reads were exported, sorted, and duplicates removed using the MarkDuplicates tool from PICARD (v2.14.0). The resulting BAM files were converted to TDF format for visualization in IGV (v2.7.2). Peak calling was conducted with MACS2 (v2.2.7) using default settings, and peaks were annotated against the mm9 genome using the annotatePeaks module in HOMER (v4.11). Heatmaps and average intensity profiles for ChIP-seq data at specific genomic regions were generated with the NGSplot program (v2.61). For spike-in samples, reads were mapped to both the mouse (mm9) and *Drosophila* (dm6) genomes. The ratio of *Drosophila* reads was used to calculate the exogenous normalization factor for each sample.

### Colony formation assay

Mouse cKit<sup>+</sup> cells were isolated from the bone marrow (BM) of WT or transgenic mice using a magnetic bead sorting system (Miltenyi Biotec) according to the manufacturer's instructions. The isolated cells (3000 per well) were plated in methylcellulose medium (M3434, StemCell Technologies) in 6-well plates containing either DMSO, 2 μM C16, or 2 μM Revumenib. Cells were cultured at 37 °C with 5% CO<sub>2</sub> for 7 days before colony enumeration and immunophenotypic analysis.

### Flow cytometric analysis

Single-cell suspensions from colonies and BM were stained with fluorochrome-conjugated antibodies. For colony immunophenotypic analysis, cells were stained with BV421-cKit, PE-cy7-Gr1 and APC-CD11b for 30 min at 4 °C. For MPP cells, LT-HSCs, ST-HSCs and BM cells were stained with APC-conjugated lineage cocktail (B220, CD4, CD5, CD8, Gr1 and Ter119), Percp-cy5.5-Sca1, BV421-cKit, PE-CD150, APC-cy7-CD48. LSK were immunophenotypically defined as Lin<sup>+</sup>cKit<sup>+</sup>Sca1<sup>+</sup>, LT-HSC as Lin<sup>+</sup>cKit<sup>+</sup>Sca1<sup>+</sup>CD48<sup>+</sup>CD150<sup>+</sup>, ST-HSCs as Lin<sup>+</sup>cKit<sup>+</sup>Sca1<sup>+</sup>CD48<sup>+</sup>CD150<sup>+</sup>, MPP as Lin<sup>+</sup>cKit<sup>+</sup>Sca1<sup>+</sup>CD48<sup>+</sup>. For committed progenitor cells, BM cells were stained with APC-conjugated lineage cocktail, Percp-cy5.5-Sca1, BV421-cKit, PE-cy7-CD16/32, PE-CD34. Granulocyte-monocyte progenitors (GMP) were immunophenotypically defined as Lin<sup>+</sup>cKit<sup>+</sup>Sca1<sup>+</sup>CD34<sup>int</sup>/CD16/32<sup>high</sup>, common myeloid progenitors (CMP) as Lin<sup>+</sup>cKit<sup>+</sup>Sca1<sup>+</sup>CD34<sup>int</sup>/CD16/32<sup>int</sup>, and megakaryocyte-erythrocyte progenitors (MEP) as Lin<sup>+</sup>cKit<sup>+</sup>Sca1<sup>+</sup>CD34<sup>int</sup>/CD16/32<sup>low</sup>. All analyses were performed using a BD FACSAria™ III cell sorter, with data processed in FlowJo software (v10).

### Mouse model and bone marrow transplantation

AE9a-transformed mouse BM cells were generously provided by Prof. Yuheng Shi. The recipient mice, at 8 weeks old, underwent sublethal irradiation (4.5 Gy) and were then transplanted with 1 × 10<sup>5</sup> BM cells via tail vein injection. The WDR5 inhibitor, C16 (WDR5-IN-1, HY-133121, MedChemExpress) was prepared as a 2 mg/mL solution in 20% 2-(hydroxypropyl)-β-cyclodextrin (HP-β-CD, HY-101103, MedChemExpress) in ddH<sub>2</sub>O. The Menin inhibitor, Revumenib was dissolved in PBS to 2 mg/mL. Mice were injected intraperitoneally at a maximum dosing volume of 5 mL/kg to give a final 10 mg/kg body weight dose. Recipient mice were maintained in an SPF facility with a 12 h light/12 h dark cycle; the room was controlled at 22 ± 2 °C and 50 ± 10% relative humidity, and standard chow and water were provided ad libitum. All animal experiments described in this study were conducted in accordance with the ethical guidelines of the Department of Laboratory Animal Science, Fudan University, China (No. 202307021S).

### Statistics and reproducibility

Western blotting and electron microscopy experiments were independently repeated twice with similar results, and representative data are shown. Phase separation assays, fluorescence recovery after

photobleaching, and immunofluorescence experiments were independently repeated three times, with similar results. The cellular phenotype of the NANOG<sup>R153A</sup> mutant was confirmed in three independent experiments.

### Ethics approval statement

All animal experiments described in this study were conducted in accordance with the ethical guidelines of the Department of Laboratory Animal Science, Fudan University, No. 202307021S.

### Reporting summary

Further information on research design is available in the Nature Portfolio Reporting Summary linked to this article.

### Data availability

The backbone chemical shifts of NANOG HD and WDR5 have been submitted to the BMRB with the accession numbers 52290 and 52291, respectively. Coordinates and structure factors of NANOG HD<sup>R100A</sup>. WDR5 complex reported in the current study have been deposited in the Protein Data Bank under accession code 8YDD. The RNA-seq and ChIP-seq data generated in this study have been deposited in the Gene Expression Omnibus (GEO) database under accession code GSE297660, GSE297961 and GSE299636. Source data are provided with this paper.

### References

- Thomson, J. A. et al. Embryonic stem cell lines derived from human blastocysts. *Science* **282**, 1145–1147 (1998).
- Keller, G. Embryonic stem cell differentiation: emergence of a new era in biology and medicine. *Genes Dev.* **19**, 1129–1155 (2005).
- Margiana, R. et al. Clinical application of mesenchymal stem cell in regenerative medicine: a narrative review. *Stem Cell Res. Ther.* **13**, 366 (2022).
- Pittenger, M. F. et al. Multilineage potential of adult human mesenchymal stem cells. *Science* **284**, 143–147 (1999).
- Chu, X. et al. Cancer stem cells: advances in knowledge and implications for cancer therapy. *Signal Transduct. Target. Ther.* **9**, 170 (2024).
- Boyer, L. A. et al. Core transcriptional regulatory circuitry in human embryonic stem cells. *Cell* **122**, 947–956 (2005).
- Ng, H. H. & Surani, M. A. The transcriptional and signalling networks of pluripotency. *Nat. Cell Biol.* **13**, 490–496 (2011).
- Young, R. A. Control of the embryonic stem cell state. *Cell* **144**, 940–954 (2011).
- Chambers, I. et al. Functional expression cloning of Nanog, a pluripotency-sustaining factor in embryonic stem cells. *Cell* **113**, 643–655 (2003).
- Pan, G. & Thomson, J. A. Nanog and transcriptional networks in embryonic stem cell pluripotency. *Cell Res.* **17**, 42–49 (2007).
- Wang, J. et al. A protein interaction network for pluripotency of embryonic stem cells. *Nature* **444**, 364–368 (2006).
- Niu, C. et al. BACH1 recruits NANOG and histone H3 lysine 4 methyltransferase MLL/SET1 complexes to regulate enhancer-promoter activity and maintains pluripotency. *Nucleic Acids Res.* **49**, 1972–1986 (2021).
- Heurtier, V. et al. The molecular logic of Nanog-induced self-renewal in mouse embryonic stem cells. *Nat. Commun.* **10**, 1109 (2019).
- Wang, J., Levasseur, D. N. & Orkin, S. H. Requirement of Nanog dimerization for stem cell self-renewal and pluripotency. *Proc. Natl. Acad. Sci. USA* **105**, 6326–6331 (2008).
- Choi, K. J. et al. NANOG prion-like assembly mediates DNA bridging to facilitate chromatin reorganization and activation of pluripotency. *Nat. Cell Biol.* **24**, 737–747 (2022).

16. Boija, A. et al. Transcription factors activate genes through the phase-separation capacity of their activation domains. *Cell* **175**, 1842–1855.e1816 (2018).
17. Sabari, B. R. et al. Coactivator condensation at super-enhancers links phase separation and gene control. *Science* **361**. <https://doi.org/10.1126/science.aar3958> (2018).
18. Liu, X. et al. Niche stiffness sustains cancer stemness via TAZ and NANOG phase separation. *Nat. Commun.* **14**, 238 (2023).
19. Ang, Y. S. et al. Wdr5 mediates self-renewal and reprogramming via the embryonic stem cell core transcriptional network. *Cell* **145**, 183–197 (2011).
20. Dou, Y. et al. Regulation of MLL1 H3K4 methyltransferase activity by its core components. *Nat. Struct. Mol. Biol.* **13**, 713–719 (2006).
21. Li, Y. et al. Structural basis for activity regulation of MLL family methyltransferases. *Nature* **530**, 447–452 (2016).
22. Dou, Y. et al. Physical association and coordinate function of the H3 K4 methyltransferase MLL1 and the H4 K16 acetyltransferase MOF. *Cell* **121**, 873–885 (2005).
23. Dias, J. et al. Structural analysis of the KANSL1/WDR5/KANSL2 complex reveals that WDR5 is required for efficient assembly and chromatin targeting of the NSL complex. *Genes Dev.* **28**, 929–942 (2014).
24. Thomas, L. R. et al. Interaction with WDR5 promotes target gene recognition and tumorigenesis by MYC. *Mol. Cell* **58**, 440–452 (2015).
25. Thomas, L. R. et al. Interaction of the oncoprotein transcription factor MYC with its chromatin cofactor WDR5 is essential for tumor maintenance. *Proc. Natl. Acad. Sci. USA* **116**, 25260–25268 (2019).
26. Sun, Y. et al. WDR5 supports an N-Myc transcriptional complex that drives a protumorigenic gene expression signature in neuroblastoma. *Cancer Res.* **75**, 5143–5154 (2015).
27. Yang, Z., Augustin, J., Hu, J. & Jiang, H. Physical interactions and functional coordination between the core subunits of Set1/MLL complexes and the reprogramming factors. *PLoS one* **10**, e0145336 (2015).
28. Hao, J. et al. A novel TOX3-WDR5-ABCG2 signaling axis regulates the progression of colorectal cancer by accelerating stem-like traits and chemoresistance. *PLoS Biol.* **21**, e3002256 (2023).
29. Ding, B. et al. WDR5 in porcine preimplantation embryos: expression, regulation of epigenetic modifications and requirement for early development\*. *Biol. Reprod.* **96**, 758–771 (2017).
30. Aho, E. R. et al. Displacement of WDR5 from chromatin by a WIN site inhibitor with picomolar affinity. *Cell Rep.* **26**, 2916–2928 e2913 (2019).
31. Grebien, F. et al. Pharmacological targeting of the Wdr5-MLL interaction in C/EBPalpha N-terminal leukemia. *Nat. Chem. Biol.* **11**, 571–578 (2015).
32. Cao, F. et al. Targeting MLL1 H3K4 methyltransferase activity in mixed-lineage leukemia. *Mol. Cell* **53**, 247–261 (2014).
33. Yu, X. et al. A selective WDR5 degrader inhibits acute myeloid leukemia in patient-derived mouse models. *Sci. Transl. Med.* **13**, eabj1578 (2021).
34. Mitchell, K. et al. WDR5 represents a therapeutically exploitable target for cancer stem cells in glioblastoma. *Genes Dev.* **37**, 86–102 (2023).
35. Abramson, J. et al. Accurate structure prediction of biomolecular interactions with AlphaFold 3. *Nature* **630**, 493–500 (2024).
36. Peng, K., Radivojac, P., Vucetic, S., Dunker, A. K. & Obradovic, Z. Length-dependent prediction of protein intrinsic disorder. *BMC Bioinforma.* **7**, 208 (2006).
37. Yang, H. et al. Generation of genetically modified mice by oocyte injection of androgenetic haploid embryonic stem cells. *Cell* **149**, 605–617 (2012).
38. Zhong, C. et al. CRISPR-Cas9-mediated genetic screening in mice with haploid embryonic stem cells carrying a guide RNA library. *Cell Stem Cell* **17**, 221–232 (2015).
39. Li, Q. et al. CRISPR-Cas9-mediated base-editing screening in mice identifies DND1 amino acids that are critical for primordial germ cell development. *Nat. Cell Biol.* **20**, 1315–1325 (2018).
40. Jauch, R., Ng, C. K., Saikatendu, K. S., Stevens, R. C. & Kolatkar, P. R. Crystal structure and DNA binding of the homeodomain of the stem cell transcription factor Nanog. *J. Mol. Biol.* **376**, 758–770 (2008).
41. Bürglin, T. R. & Affolter, M. Homeodomain proteins: an update. *Chromosoma* **125**, 497–521 (2016).
42. Yang, Y. et al. Structural studies of WDR5 in complex with MBD3C WIN motif reveal a unique binding mode. *J. Biol. Chem.* **300**, 107468 (2024).
43. Hayashi, Y. et al. Structure-based discovery of NANOG variant with enhanced properties to promote self-renewal and reprogramming of pluripotent stem cells. *Proc. Natl. Acad. Sci. USA* **112**, 4666–4671 (2015).
44. Murakami, K. et al. NANOG alone induces germ cells in primed epiblast in vitro by activation of enhancers. *Nature* **529**, 403–407 (2016).
45. Sun, Y. et al. STING is crucial for the survival of RUNX1::RUNX1T1 leukemia cells. *Leukemia* **38**, 2102–2114 (2024).
46. Tian, J. et al. Discovery and structure-based optimization of potent and selective WD repeat domain 5 (WDR5) inhibitors containing a dihydroisoquinolinone bicyclic core. *J. Med. Chem.* **63**, 656–675 (2020).
47. Issa, G. C. et al. The menin inhibitor revumenib in KMT2A-rearranged or NPM1-mutant leukaemia. *Nature* **615**, 920–924 (2023).
48. Lu, Y. et al. Phase separation of TAZ compartmentalizes the transcription machinery to promote gene expression. *Nat. Cell Biol.* **22**, 453–464 (2020).
49. Hu, H. et al. Evaluation of the determinants for improved pluripotency induction and maintenance by engineered SOX17. *Nucleic Acids Res.* **51**, 8934–8956 (2023).
50. Solvie, D. et al. MYC multimers shield stalled replication forks from RNA polymerase. *Nature* **612**, 148–155 (2022).
51. Pei, X. et al. E242-E261 region of MYC regulates liquid-liquid phase separation and tumor growth by providing negative charges. *J. Biol. Chem.* **300**, 107836 (2024).
52. Guo, L. et al. Nuclear-import receptors reverse aberrant phase transitions of RNA-binding proteins with prion-like domains. *Cell* **173**, 677–692.e620 (2018).
53. Yu, H. et al. HSP70 chaperones RNA-free TDP-43 into anisotropic intranuclear liquid spherical shells. *Science* **371**. <https://doi.org/10.1126/science.abb4309> (2021).
54. Carugo, A. et al. In vivo functional platform targeting patient-derived xenografts identifies Wdr5-myc association as a critical determinant of pancreatic cancer. *Cell Rep.* **16**, 133–147 (2016).
55. Minor, W., Cymborowski, M., Otwinowski, Z. & Chruszcz, M. HKL-3000: the integration of data reduction and structure solution—from diffraction images to an initial model in minutes. *Acta Crystallogr. D. Biol. Crystallogr.* **62**, 859–866 (2006).
56. Storoni, L. C., McCoy, A. J. & Read, R. J. Likelihood-enhanced fast rotation functions. *Acta Crystallogr. D. Biol. Crystallogr.* **60**, 432–438 (2004).
57. Schuetz, A. et al. Structural basis for molecular recognition and presentation of histone H3 by WDR5. *EMBO J.* **25**, 4245–4252 (2006).
58. Adams, P. D. et al. PHENIX: a comprehensive Python-based system for macromolecular structure solution. *Acta Crystallogr. D. Biol. Crystallogr.* **66**, 213–221 (2010).
59. Emsley, P., Lohkamp, B., Scott, W. G. & Cowtan, K. Features and development of Coot. *Acta Crystallogr. D. Biol. Crystallogr.* **66**, 486–501 (2010).
60. Salzmann, M., Pervushin, K., Wider, G., Senn, H. & Wuthrich, K. TROSY in triple-resonance experiments: new perspectives for

- sequential NMR assignment of large proteins. *Proc. Natl. Acad. Sci. USA* **95**, 13585–13590 (1998).
61. Delaglio, F. et al. NMRPipe: a multidimensional spectral processing system based on UNIX pipes. *J. Biomol. NMR* **6**, 277–293 (1995).
  62. Lee, W., Tonelli, M. & Markley, J. L. NMRFAM-SPARKY: enhanced software for biomolecular NMR spectroscopy. *Bioinformatics* **31**, 1325–1327 (2015).
  63. Kazimierczuk, K. & Orekhov, V. Y. Accelerated NMR spectroscopy by using compressed sensing. *Angew. Chem. Int. Ed. Engl.* **50**, 5556–5559 (2011).
  64. Orekhov, V. Y. & Jaravine, V. A. Analysis of non-uniformly sampled spectra with multi-dimensional decomposition. *Prog. Nucl. Magn. Reson. Spectrosc.* **59**, 271–292 (2011).
  65. Fan, R. et al. Wnt/Beta-catenin/Esrrb signalling controls the tissue-scale reorganization and maintenance of the pluripotent lineage during murine embryonic diapause. *Nat. Commun.* **11**, 5499 (2020).

## Acknowledgements

We thank Prof. Jinsong Li for providing AG-haESCs. We are grateful to the staff of the BL19U1 beamline of the National Facility for Protein Science Shanghai (NFPS) at Shanghai Synchrotron Radiation Facility (SSRF) for X-ray diffraction data collection. We also thank the staff members of the Large-scale protein preparation system (<https://cstr.cn/31129.02.NFPS.LSPS>), the nuclear magnetic resonance system, and the integrated laser microscopy system at NFPS, Shanghai Advanced Research Institute, Chinese Academy of Science, for providing technical support and assistance in data collection and analysis. This work was supported by grants from the National Natural Science Foundation of China (32471528 and 32071195 to Y.L., 32300480 to D.W., 82400135 to J.X.), the State Key Laboratory of Systems Medicine for Cancer (zz-RCPY-23-25 and zz-94-25-22 to Y.L.), the Shanghai Rising-Star Program (23QC1400600 to Y.L.), the Shanghai Oriental Talent Youth Program (DFYC-LYJ2022 to Y.L.), the National Key Research and Development Program of China (2023YFA1800403 to Y.C.), Shanghai Pilot Program for Basic Research -CAS Shanghai Branch (JCYJ-SHFY-2022-008 to Y.C.), the Shanghai Sailing Program (22YF1453800 to D.W.), the China Postdoctoral Science Foundation (2022M710145 to D.W.), the 2024 National Clinical Key Specialty Construction Project (10000015Z155080000004) and the Jiading district medical key discipline construction project (XK202401). D.W. gratefully acknowledges the support of Heye and Sanofi Scholarship Program.

## Author contributions

Y.Li and Y.C. conceived and supervised the project. D.W. performed phase separation assays and Co-IP experiments. X.S. and Q.D. conducted ESC-based functional assays and carried out ChIP-seq and RNA-

seq analyses. J.X. and Y.S. performed LSC-related functional validation, Y.Li and L.Z. purified the proteins, carried out crystallization and structural determination. B.W. and H.X. carried out NMR experiments. Y.H. performed EM experiments. J.S., X.W., B.H., and S.Y. assisted in data processing and interpretation. Y.Liu, J.W., Y.C. and Y.Li designed the experiments and interpreted the results. D.W., X.S., J.X., L.Z., B.W., Y.S., Y.Liu, J.W., Y.C. and Y.Li prepared the figures and wrote the manuscript.

## Competing interests

The authors declare no competing interests.

## Additional information

**Supplementary information** The online version contains supplementary material available at <https://doi.org/10.1038/s41467-026-68623-w>.

**Correspondence** and requests for materials should be addressed to Yingbin Liu, Jianlong Wang, Yong Chen or Yanjing Li.

**Peer review information** *Nature Communications* thanks the anonymous reviewers for their contribution to the peer review of this work. A peer review file is available.

**Reprints and permissions information** is available at <http://www.nature.com/reprints>

**Publisher's note** Springer Nature remains neutral with regard to jurisdictional claims in published maps and institutional affiliations.

**Open Access** This article is licensed under a Creative Commons Attribution-NonCommercial-NoDerivatives 4.0 International License, which permits any non-commercial use, sharing, distribution and reproduction in any medium or format, as long as you give appropriate credit to the original author(s) and the source, provide a link to the Creative Commons licence, and indicate if you modified the licensed material. You do not have permission under this licence to share adapted material derived from this article or parts of it. The images or other third party material in this article are included in the article's Creative Commons licence, unless indicated otherwise in a credit line to the material. If material is not included in the article's Creative Commons licence and your intended use is not permitted by statutory regulation or exceeds the permitted use, you will need to obtain permission directly from the copyright holder. To view a copy of this licence, visit <http://creativecommons.org/licenses/by-nc-nd/4.0/>.

© The Author(s) 2026

<sup>1</sup>State Key Laboratory of Systems Medicine for Cancer, Shanghai Cancer Institute, Renji Hospital Affiliated to Shanghai Jiao Tong University School of Medicine, Shanghai, China. <sup>2</sup>Key Laboratory of Epigenetic Regulation and Intervention, Shanghai Institute of Biochemistry and Cell Biology, Center for Excellence in Molecular Cell Science, Chinese Academy of Sciences; University of Chinese Academy of Sciences, Shanghai, China. <sup>3</sup>Department of Medicine, Columbia Center for Human Development and Stem Cell Therapies, Columbia University Irving Medical Center, New York, NY, USA. <sup>4</sup>Shanghai Key Laboratory of Cancer System Regulation and Clinical Translation (CSRCT-SHANGHAI), Jiading District Central Hospital, Shanghai, China. <sup>5</sup>Protein Data Bank China (PDBc), Shanghai Advanced Research Institute, CAS, Shanghai, China. <sup>6</sup>Department of Thyroid and Neck Cancer, Tianjin Medical University Cancer Institute and Hospital, National Clinical Research Center for Cancer, Key Laboratory of Cancer Prevention and Therapy, Tianjin's Clinical Research Center for Cancer, Tianjin, China. <sup>7</sup>Institute of Microsurgery on Extremities, Department of Orthopedic Surgery, Shanghai Sixth People's Hospital Affiliated with Shanghai Jiao Tong University School of Medicine, Shanghai, China. <sup>8</sup>National Facility for Protein Science in Shanghai, Zhangjiang Lab, Shanghai Advanced Research Institute, Chinese Academy of Science, Shanghai, China. <sup>9</sup>Center of Precision Medicine for Blood Diseases, Huashan Hospital, Zhongshan-Xuhui Hospital, Shanghai Key Laboratory of Medical Epigenetics, Institutes of Biomedical Sciences, Medical College of Fudan University, Shanghai, China. <sup>10</sup>These authors contributed equally: Duo Wang, Xianle Shi, Jiaying Xie, Lijie Zhao, Bin Wu. ✉ e-mail: [laoniulyb@shsmu.edu.cn](mailto:laoniulyb@shsmu.edu.cn); [jw3925@cumc.columbia.edu](mailto:jw3925@cumc.columbia.edu); [yongchen@sibcb.ac.cn](mailto:yongchen@sibcb.ac.cn); [liyanjing@sjtu.edu.cn](mailto:liyanjing@sjtu.edu.cn)